

POLITECNICO DI TORINO

AUTOMOTIVE ENGINEERING

CORSO DI LAUREA IN
INGEGNERIA DELL'AUTOVEICOLO



Tesi di Laurea Magistrale

**Structural Validation of Hanger Brackets
in Exhaust Systems: Correlation Between
Virtual Simulation and Experimental
Testing and Its Optimization**

Relatore: Prof. Andrea Tonoli

Tutor: Ing. Marco Nardi

Candidato: Alex Giovinazzo

Aprile 2019

To my parents.

Abstract

Since the last decades, the engineering design activity has shifted from manual drawings and dimensioning calculations to their computer-aided versions.

Nowadays, in the industrial field, any manufactured product, as well as its characteristics and the operational processes necessary to build it, is designed and simulated in advance exploiting the computational capabilities of computers. By virtue of this technological improvement, design modifications are applied easily and their effects are checked instantaneously, allowing a reduction of the product development time. Once the iterative adaptation process has finished, the project is validated.

Although virtual analysis results, manufactured goods have to be tested in a physical manner to confirm that the final objects comply with the imposed requirements. Here, a second validation arises.

As a matter of fact, the two validation methods differ because of the impossibility of replicating identically the physical test in a virtual environment. To overcome this obstacle, simplifying assumptions are considered, but this unavoidably creates differences.

The aim of this Thesis project is to analyze the two structural validation methods (experimental and virtual) to understand the dissimilarities and the effects that they exert on the correlation and to propose new validation procedures that provide more correlated results between the two methodologies.

The present work is the summary of six months of internship within the Exhaust Systems R&D Testing department at Magneti Marelli S.p.A., an Italian industry with worldwide diffusion devoted to the production of automotive components. The focuses of the investigation are the structural validation methods of hanger brackets in exhaust systems.

After the introduction of the state-of-the-art methods adopted by the Company for the fatigue life validation in exhaust hanger brackets, a complete case study analysis provides the evidence of the inconsistencies related to the procedures. Different alternatives to the usual methods are proposed: evaluation of load levels on each bracket equivalent to the experimental driving test, different computational validation method based on structural vibrational analysis and identification of an average cumulative load curve, reveal to reduce the gap between the methodologies. Eventually, some guidelines for the verification and application of the innovative validation dispositions are proposed.

Contents

1	Introduction	1
1.1	The Exhaust System: an overview	1
1.2	Purpose of the work	4
1.3	Design and Validation Methods	6
1.4	List of the exhaust systems analysed	7
1.4.1	Model 356	7
1.4.2	Model 520 without muffler	8
1.4.3	Model 520 with rear muffler	8
1.4.4	Model 952	9
2	Virtual validation	10
2.1	Model preparation and Mesh	11
2.2	Damage evaluation: Road Load Simulation	15
3	Experimental validation	19
3.1	Fatigue test and Wöhler's curve computation	20
3.2	Data acquisition on the Proving Ground	22
3.2.1	Test exhaust line preparation	23
3.3	Data analysis and comparison with Wöhler's curve	27
3.3.1	Strain gauges calibration	27
3.3.2	Damage evaluation and Validation criterion	30
4	Equivalent load	32
4.1	Differences between the methods	32
4.1.1	Correlation proposals	33
4.2	Equivalent load	33
4.2.1	Objective	33
4.3	Input data	34
4.4	Computation	35
4.5	Results comparison	36
4.5.1	Virtual calibration	37
4.5.2	Computation of the brackets loads	40
4.6	Comment and critical issues	40

5	Vibrational analysis	44
5.1	Initial observations	44
5.2	Procedure	45
5.2.1	Calibration at the Road Simulation Bench	48
5.2.2	Virtual Vibrational analysis	51
5.3	Results comparison	53
5.3.1	Simulation of road acceleration spectra	53
5.3.2	Modal deformation	55
5.4	Comments and observations	63
6	Global cumulative curve	65
6.1	Procedure	65
6.2	Result	66
7	Conclusion	68
A	Strain calibration factors	69
B	Road Simulation Bench description	71
	Bibliography	73

List of Figures

1.1	Exhaust line subdivision into Hot-End and Cold-End	3
1.2	Monolith flow distribution	3
1.3	Exhaust muffler components nomenclature	5
1.4	Exhaust line under-body constraints	6
1.5	Steps in the validation process	7
1.6	Layout of the 356 line	7
1.7	Layout of the 520 line without muffler	8
1.8	Layout of the 520 line with muffler	8
1.9	Layout of the 952 line	9
2.1	Bracket and weld bead mesh	12
2.2	Mesh of a junction between two surfaces	12
2.3	<i>CBUSH</i> and <i>Rigids</i> employment in FE analysis	13
2.4	Converters substrates internal structure	14
2.5	Haigh diagram working point identification	15
2.6	Graphical representation of Safety Factor	16
2.7	Haigh diagram of base and welded material and temperature effect	17
2.8	Stress and Safety Factor maps	18
3.1	Sinusoidal symmetric load	21
3.2	Hydraulic jack	21
3.3	Wöhler's curve from fatigue test	22
3.4	Gas deviation upstream Cold-End	23
3.5	Gas deviation downstream SCRUF	24
3.6	Scheme of a strain gauge	24
3.7	Strain gauges positioning	25
3.8	Strain gauges electrical connection	26
3.9	Strain gages calibration bench	28
3.10	Calibration strain time history	28
3.11	Load-Strain calibration characteristic	29
3.12	Strain-to-Load time history conversion	29
3.13	Graphical representation of Miner's equation components	30

4.1	Different strain (or load) cycles	34
4.2	Equivalent load graphical representation	36
4.3	Virtual calibration constraints	37
4.4	Stress experimental calibration	38
4.5	Correspondence of stress measurement points	39
4.6	Scheme of bracket load computation from stress map	40
4.7	Equivalent loads-to-Mass ratios	43
5.1	Under-body and brackets accelerometers	45
5.2	Road acceleration spectra (FFT)	47
5.3	Road Simulation Bench	48
5.4	RSB reproduced counter-bracket	49
5.5	Exhaust line mounted on RSB	50
5.6	Rubber isolators dynamic stiffness	51
5.7	Rubber isolators damping coefficient variation	52
5.8	FEM accelerations application points	53
5.9	Comparison between experimental outcomes and numerical vi- brational analysis	55
5.10	RSB acceleration spectra (FFT)	56
5.11	Composition of a colour map	57
5.12	Proving Ground surface	57
5.13	356 - Colour maps of tailpipe bracket acceleration and deformation	58
5.14	356 - Modal shape at 18.5 Hz	59
5.15	356 - Colour maps of penultimate bracket acceleration and de- formation	60
5.16	356 - Modal shape at 13.1 Hz	60
5.17	520- Colour maps of penultimate bracket acceleration and de- formation	61
5.18	520 - Modal shape at 10.1 Hz	61
5.19	263 - Colour maps of tailpipe bracket acceleration and deformation	62
5.20	263 - Modal shape at 22.8 Hz	62
6.1	Superposition of normalized cumulative curves	66
6.2	Global normalized cumulative curve	67
B.1	Road Simulation Bench	72

List of Tables

4.1	Differences between validating methods	33
4.2	Example of table for the computation of Equivalent loads	36
4.3	Comparison between experimental and virtual stress calibration	39
4.4	Comparison between Equivalent an $4g$ -caused brackets loads	40
5.1	Acceleration spectra matrix for each pavement	46
5.2	Comparison between isolators and brackets maximum forces	55
5.3	Comparison of experimental and vibrational simulation outcomes	63
A.1	520 - Strain calibration coefficients	69
A.2	356 - Strain calibration coefficients	70

List of Acronyms

CAD	Computer Aided Design
CAE	Computer Aided Engineering
CE	Cold-End
HE	Hot-End
ECU	Engine Control Unit
DV	Design Validation
PV	Product Validation
FE	Finite Element
FEA	Finite Element Analysis
RLDA	Road Load Data Acquisition
SF	Safety Factor
DAQ	Data Acquisition system
MIL	Malfunction Indication Lamp
SCR	Selective Catalytic Reduction
DPF	Diesel Particulate Filter
EMI	Electro-Magnetic Interferences
RSB	Road Simulation Bench
FFT	Fast Fourier Transform

List of Symbols

f	Frequency [Hz]
g	Gravity acceleration [9.81 m/s ²]
A, B	Wöhler's curve parameters
R	Electric resistance [Ω]
ΔR	Electric resistance variation
ε	Material strain
K_s	Strain gauge resistance factor
l	Generic length
Δl	Length variation
$\mu strain$	Practical measurement unit of the mechanical strain [$\mu\text{m}/\text{m}$]
F_i	Generic force/load
d_i	Damage contribution of the load level F_i
n_i	Number of counted occurrences of the load F_i
N_i	Number of repetitions of load F_i that leads to component failure
D	Damage according to Miner's rule
F_{eq}	Equivalent load
n_{eq}	Equivalent number of cycles
N_{eq}	Number of repetitions of load F_{eq} at failure
$E 1 \div 4$	Indication of the polar location around a bracket
σ	Statistical standard deviation

Chapter 1

Introduction

1.1 The Exhaust System: an overview

In the past, the exhaust system of a vehicle was merely considered as the set of elements aimed at collecting burnt gases from the engine outlet ports and dispersing them towards the environment, in a way that minimized the interaction with the occupants. Indeed, the exhaust pipes of passenger cars end typically behind the vehicle, in a position close to the ground, whilst in some industrial vehicles vertical ducts discharge combustion gases above the vehicle roof, to avoid gas recirculation in the cabin even in case of stationary operations (e.g. earth moving machines). This is fundamental because combustion products contain toxic substances, like carbon monoxide (CO), benzene or nitrogen oxides (NO_x), which are harmful for human beings and may lead to a loss of consciousness if inhaled in high concentration.

In the last decades, this mere transportation purpose has been flanked by several further roles, some of which gained a preponderant place over the others. In particular, the new implemented functions are, following a hierarchical order:

- abatement of the pollutants deriving from the non-ideal combustion processes that occur in the engine, through chemical catalysis of the exhaust gas stream;
- tailpipe noise, principally deriving from combustion events, and shell noise reduction, in order to achieve type-approval acoustic limitations and to improve internal comfort;
- minimization of the resistance the exhaust gas has to face in crossing the pipes, mainly caused by internal elements (catalytic converters, filters and traps, muffler diaphragms, flow interaction, etc.) to avoid an engine throttling effect and a reduction of its volumetric efficiency;

- thermal insulation between hot parts, in particular manifolds and catalytic converters, and nearby components, employing heat shields;
- vibration insulation between the suspended line and the chassis, made through rubber isolators, to enhance riding comfort;
- aesthetic appearance, provided by chromed stainless steel tailpipe terminations;
- in particular applications, like sport cars, the exhaust system is shaped in order to convert the combustion noise into a specific "sound", which imparts the vehicle a distinctive personality, still respecting noise limitations imposed by the legislation.

Since many of these characteristics are fundamental for correct vehicle operation, as well as for its commercialization, it is of paramount importance to preserve all them during the entire vehicle life span. This is a challenging goal because, although the high level requirements imposed by the customer (namely the car maker), the price of the entire system must be kept as low as possible. Albeit this marketing rule applies to any type of product and goods, in the specific case of the exhaust system it is particularly important because, in the final customer's mind (typically the driver/owner), the exhaust does not carry any added value to the vehicle, thus he is not willing to spend further money for special components, even if they are guaranteed to withstand highly severe conditions.

Furthermore, the working environment of the system is adverse: water, de-icing salt, stones, etc. are elements that impact unavoidably with the exhaust line during normal vehicle operations. For this reason, the definition of the system must be carried with the objectives in mind. The design is even more complicated by the narrow space available in the under-body: suspension assembly, shafts and axles, fuel/urea tanks and rear bumper are all elements that reside close to the exhaust, but that must not interfere with it. That is the reason of the complex shapes given to the piping: they must fit the available space, not protruding in the internal compartment volume.

In view of the very different objectives that an exhaust system has to accomplish and of the different boundary conditions to which the line is subjected, it is usual to subdivide it into two sections (Figure 1.1):

- Hot-End (HE);
- Cold-End (CE).

The former, as the name suggests, is the first tract of the line, from the engine outlet ports, up to the flexible joint. The elements belonging to this subgroup have to cope with hot and aggressive gas either for its collection from

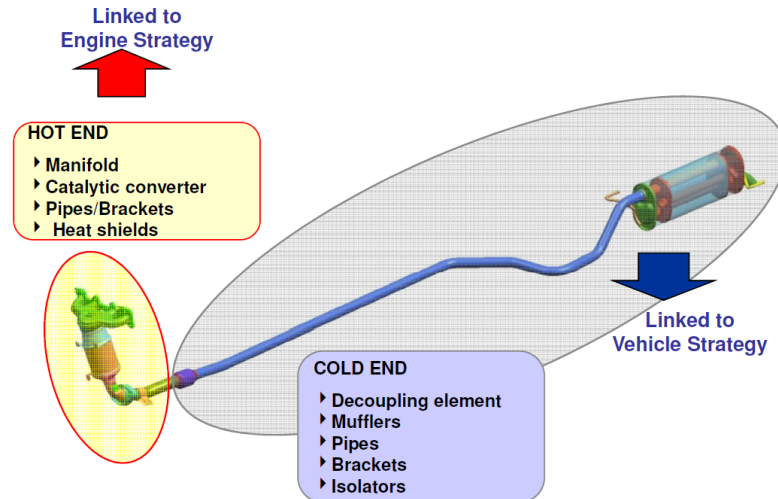


Figure 1.1: Exhaust line subdivision into Hot-End and Cold-End and related components belonging to each subgroup

the engine (exhaust manifold and piping) and for the promotion of chemical reactions (catalytic converters and filters). Because of the extreme temperature involved, which can reach almost $1\,000^{\circ}\text{C}$ in high performance sport cars, and of the high vibration levels transmitted by the engine head, Hot-End components must be designed to withstand infinite thermo-mechanical fatigue in a corrosive environment. Moreover, exhaust manifolds are designed to avoid cross-flow among the ducts, whilst conical tracts of converters housings are shaped in a way that distributes evenly the gas over the inlet surface of the monolith, to maximize the conversion efficiency: accurate fluid-dynamic analyses reveal to be fundamental for these components.

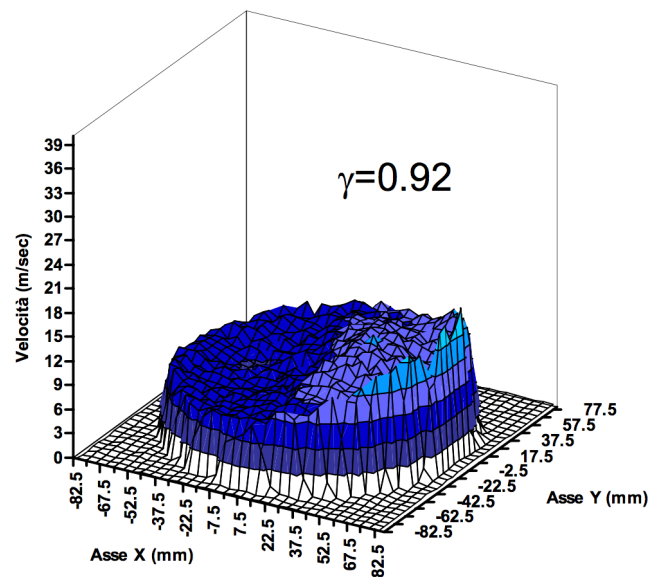


Figure 1.2: Example of flow distribution analysis on a converter monolith

To sum up, since this subset integrates, further to the piping, some chemical structures and electronic devices, able to cope with the engine control unit (ECU) to apply the best injection strategies, its design is mainly related to engine requirements, hence it is very often carried along with the car maker or in a joint-venture with the engine manufacturer.

The Cold-End subgroup, by convention, starts downstream the flexible decoupler and includes all the components up to the tailpipe. The main constituents of this sub-assembly are the mufflers, the pipes, the hanger brackets and the elastic isolators with which the line is anchored to the vehicle under-body. Although the gas may reach the environment with a temperature significantly higher than the atmospheric one, in the order of $90 \div 100^\circ\text{C}$ at maximum, the designation of *cold* indicates that the thermal effects on the components are negligible with respect to mechanical stresses. As a matter of fact, every analysis and experimental test made on these elements is carried at room temperature, with paltry effects on the results.

The Cold-End design is principally depending on vehicle strategy. As explained, the main drivers of the project, especially for conventional cars, are internal comfort and available space present in the under-body, always considering cost minimization. This leads to the reduction of components redundancy, like silencers, by properly shaping few key elements. On premium cars, the Cold-End is also responsible of imparting a distinctive "personality" to the vehicle. Chromed tailpipe terminations and a deep exhaust sound provide good appearance and pleasant feeling to the driver, of course at an higher production cost.

1.2 Purpose of the work

The following dissertation collects and synthesizes the results and the experiences of a six-months internship in the R&D Testing Department of the Exhaust Systems division of Magneti Marelli S.p.A. in Venaria Reale, Turin (Italy). The Company has numerous plants diffused all over the world which design and produce several automotive spare parts and components, among which also exhaust systems.

The proposed Thesis is focused on the analysis optimization of some components belonging to the Cold-End segment of the exhaust system. Particular attention has been dedicated to structural validation of hanger brackets. The outcomes of this activity could be adapted to other elements of the line, for instance welded junctions between pipes and muffler end caps, for which similar validation procedures are employed.

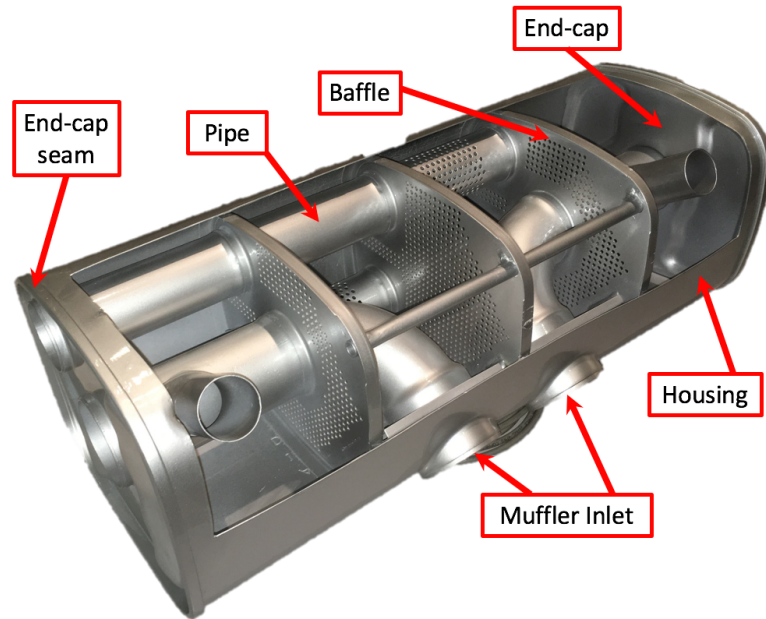


Figure 1.3: *Nomenclature of exhaust muffler components*

More in depth, the cardinal objective of the investigation is to identify an innovative virtual validation method featuring a better correlation with the experimental test. In fact, at the present time, fatigue life accreditation on these components is based on best practices, explained in Chapters 2 and 3, established by the Company in accordance with the customers. Although these standards revealed to be satisfactory in guaranteeing components resistance all along vehicle service life, the research has been carried to reduce the discrepancies that exist between virtual and experimental methods, in such a way that both lead to comparable results.

All the analyses and conclusions proposed are the outcomes of physical tests that the author had the opportunity to set up and perform on the exhaust lines of some models and the elaboration of data gathered by him and by the Company on previous projects. Several approaches, explained in the details in Chapter 4.1.1, have been undertaken and their results have been examined to identify the best fitting technique. Further to this, the same analyses have been conducted on exhaust systems of various cars and the results have been compared among each other with the intention of discovering some relations with a global validity and not merely tailored on a specific case study.

Eventually, further to the interim conclusion reached at the end of the traineeship period, an insight into possible open points worthy to be developed will be proposed.

1.3 Design and Validation Methods

The responsibility of an exhaust systems' manufacturer is to design and produce exhaust lines that achieve the requirements imposed by the customer, typically a car maker. Usually, the project starts with the recognition of topological boundary conditions of the vehicle under-body, namely the available space, the location of the mounts, the presence of components sensible to the temperature and so forth, which are depicted in Figure 1.4.



Figure 1.4: Scheme of the main constraints on the design of the exhaust line in a vehicle under-body

Subsequent to the geometrical definition, the exhaust line properties and behaviours have to be verified and the model characteristics modulated with the aim of respecting the requisites stipulated in the contract with the customer. In a first phase, the verification is carried out in a virtual manner, employing *CAD/CAE* methods. Thereafter, the first prototypes are built and the design adequacy is assessed by means of physical tests, the results of which will determine if the project has to be revised.

Finally, once the design has been thoroughly validated, the mass production can start. However, the release of this acknowledgement does not imply that the produced elements will be immune from errors: some components, extracted randomly from the line, are subjected to a further set of tests, similar to the validating ones, whose purpose is to certify that the production processes are suitable to manufacture components that fulfil the requirements agreed. In Figure 1.5 the principal steps of the validating processes are illustrated.

As it can be easily inferred, the former step is called *Virtual validation*, whilst the latter two fall under the name of *Experimental validation* of the *Design* (DV) and of the final *Product* (PV). In the following Chapters, both methods will be described in their details, dedicating a particular attention to the application of them for hanger brackets fatigue life validation.

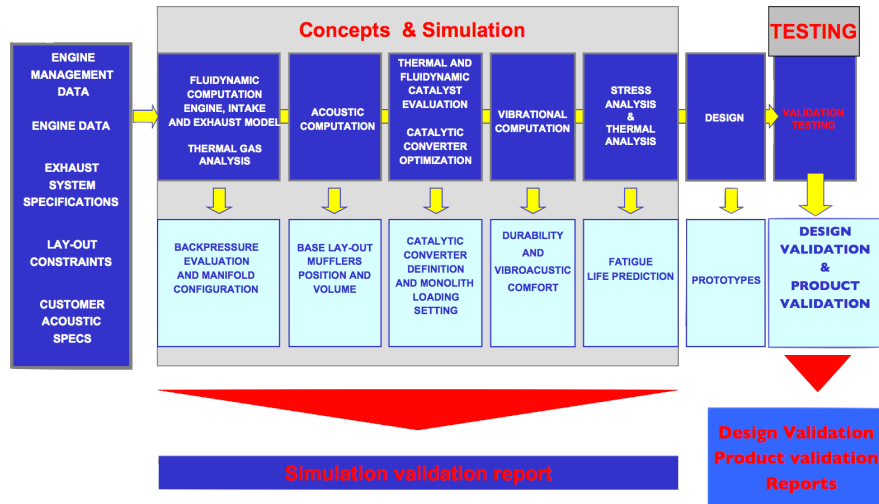


Figure 1.5: Summary of the characteristics inspected during the validation processes, arranged in a chronological order. On the left of the Figure there are the design inputs/boundary conditions

1.4 List of the exhaust systems analysed

In this Section, the layouts of the principal exhaust lines analysed are listed as reference for the results proposed. For all the models, the experimental investigation has been supported by, and the results compared to, computational simulations.

For all the vehicles, only the project number is reported, neglecting the commercial name.

1.4.1 Model 356

The exhaust system shown in Figure 1.6 has been thoroughly scrutinized by the author, as fundamental case-study. From the application of strain gauges and under-vehicle accelerometers, the line has been tested on the prescribed Proving Grounds, to be finally analysed at the Road Simulation Bench.



Figure 1.6: Layout of the line belonging to the model 356

Data concerning the subsequent models, on the contrary, were already available in the Company. They have been elaborated and analysed to be compared with the results of the case-study. Nevertheless, for calibration purposes, some

extra strain gauges (principally rosettes) have been applied also to some of these systems.

1.4.2 Model 520 without muffler

For the line presented in Figure 1.7, both brackets strains and counter-brackets accelerations have been acquired to try to discover a relation among them.

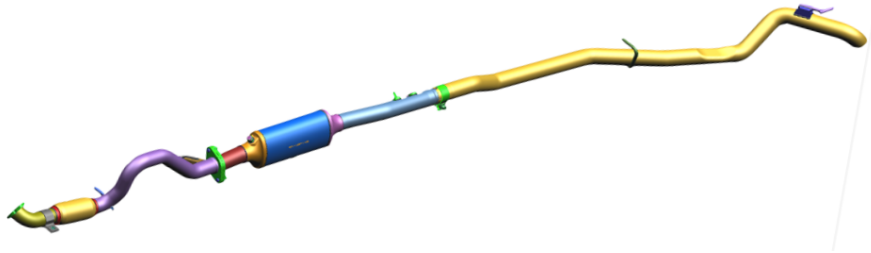


Figure 1.7: *Layout of the line belonging to one model 520*

1.4.3 Model 520 with rear muffler

This layout, reported in Figure 1.8, has been mainly employed for calibration purposes and for understanding the relation between equivalent loads at the brackets and line mass distribution.

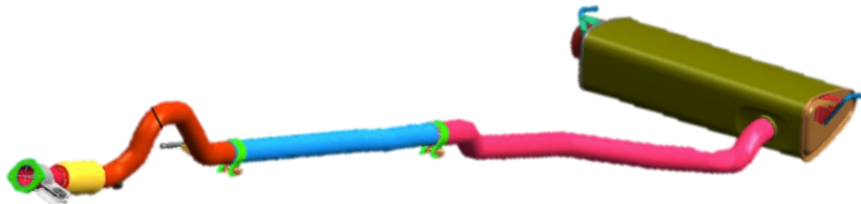


Figure 1.8: *Layout of the line belonging to another model 520, endowed with the rear muffler*

1.4.4 Model 952

Data related to the exhaust line of Figure 1.9, similarly to the previous case, have been analysed in terms of equivalent loads, in relation to the different layouts.

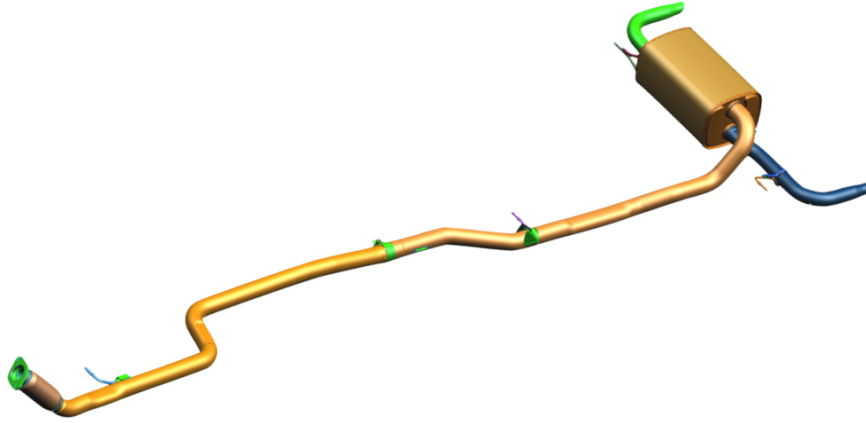


Figure 1.9: *Layout of the line belonging to the model 952*

Lastly, for the evaluation of a global cumulative proposed in Chapter 6, data of 156 brackets of different models and layouts, collected by the Team during its testing activities, have been inferred in a statistical perspective. Still, none of them has been scrutinized with unconventional methods other than the agreed validating procedure.

Chapter 2

Virtual validation

Once the topological design of the exhaust line has been completed by the drawing team, a set of virtual analyses is run on it, as evidenced in Figure 1.5. The aim of such an examination is to ascertain, before the production, that the components will respect the targets imposed by the customer, thus avoiding wasting time and money in manufacturing not compliant parts. The characteristics of the exhaust systems that are checked are, among all:

- Fluid-dynamic behaviour, mainly of the Hot-End group, but also of the whole assembly, to evaluate the back-pressure that the gases would face while crossing the exhaust;
- Acoustic response of the line, to understand if the adoption of mufflers is mandatory, and eventually to determine their dimensions;
- Catalyst surface exploitation (see Figure 1.2) and conversion efficiency determination to establish the required monolith's precious metal loading to achieve the emissions target;
- Mode Shapes of the line, through a modal analysis at room temperature, to evidence the natural deformations of the system;
- Natural Frequencies of the exhaust system, second outcome of the modal analysis. For the Hot-End, the eigenfrequencies must lay above the excitation spectrum produced by the engine, while for the Cold-End, the customer requirements focus usually on hanger brackets' natural frequencies rather than on the whole line;
- Rubber Isolators Reliability, to ensure that the static loads on the elastic elements due to gravity are below the acceptable thresholds;
- Cold-End Containment, to verify that the application of 1 g vertical (Z) and lateral (Y) static accelerations does not lead to interferences with chassis components and rear bumper;

- Thermal Stresses, through a thermal analysis, especially for the Hot-End, to ensure that stresses due to thermal elongation do not overcome material limits;
- Fatigue behaviour, both for the Hot-End, which has to sustain infinite fatigue life, and for the Cold-End. The latter is inspected through a damage evaluation or Road Load Simulation, either for the single brackets and for the whole sub-assembly, to evaluate the damage level of the components when subjected to established loads.

Going deeper in the details of the last point, which is the core of this Thesis work, fatigue verification, at this stage, is made comparing local stresses on the exhaust line generated by the application of a predefined load, to the fatigue limit of the **material**, obtained from the corresponding Haigh diagram. From the ratio of these values, a Safety Factor (SF) for each node of the Finite Element (FE) model is obtained. In the following Sections, a better explanation of these processes will be proposed.

2.1 Model preparation and Mesh

For running the computational simulation, it is necessary to assign material properties to the various components, starting from the input geometry, designed by the drawing team, and to mesh the parts. Then, according to the type of analysis to be carried, proper boundary conditions (namely constraints) and external inputs (normally forces, displacements, accelerations, temperatures, etc.) are applied to the model.

At this point, the solver is launched and the results of the computation are visualized in the post-processing phase.

Conventionally, the Finite Element Analysis (FEA) applied to exhaust systems' Cold-Ends employs four types of elements:

- 3D *Hexa* elements, featuring a parallelepiped shape, for hanger brackets. Since first order elements are used, meaning that local stress and strain have a constant value within the element, to describe the internal stress distribution (butterfly diagram) of the structure it is necessary to map the thickness of these features with two rows of *hexa* elements, as shown in Figure 2.1;
- 3D *Penta* elements, prisms with triangular base, for most of the weld beads. This strategy is both used for the junctions between two solid bodies and between a solid and a surface;

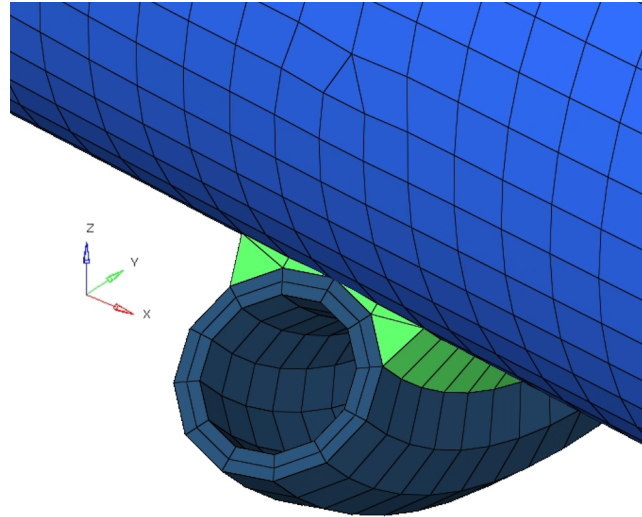


Figure 2.1: *Enlargement of the welded connection between bracket and pipe. It is clearly visible the two-layer mapping of the former and the triangular base of green Penta elements used to model the weld bead*

- 2D *Shell* elements for pipes, muffler housings, end-caps, internal baffles, etc., subdivided in their turn into *Tria* (triangles) and *Quad* (quadrilaterals). In this case, the material thickness is assigned symmetrically with respect to the base surface of the drawing. Furthermore, these elements are employed to model the junction between two surfaces, as represented in Figure 2.2: in this case, the weld bead is simulated connecting the nodes of the two shells by means of a set of *rigids* and covering the gap with an additional oblique surface (a *shell*) that represents the actual surface of the bead.

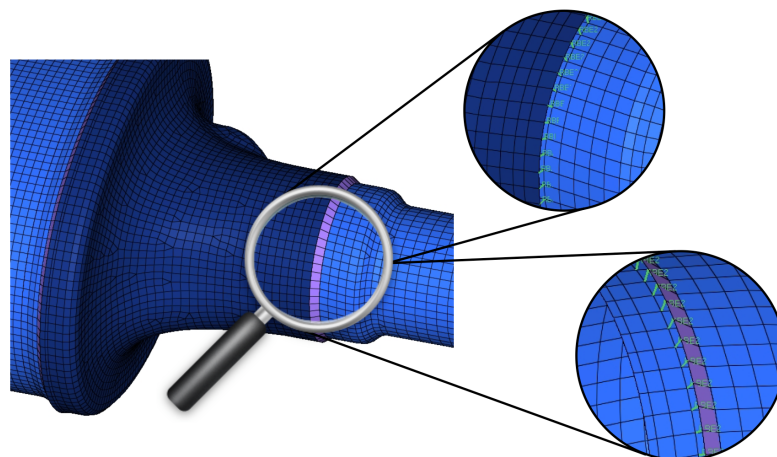


Figure 2.2: *Highlight of the modelling of welded junction between two surfaces. The green sticks, labelled "RBE2", are the rigids, while the purple inclined surface represents the weld bead.*

- *CBUSH* elements for flexible decoupler and rubber isolators. This element, featuring the same behaviour of a spring, concentrates its stiffness property, with its relative value depending on the direction, between its extremities. These nodes are connected to the adjacent components (pipes in case of flexible decoupler, brackets and counter-brackets for rubber isolators) through *rigids*, in such a way that their relative displacement is transferred identically to the extremities of the aforementioned elastic element.
- *Rigids* elements, as announced before, used to simulate infinitely stiff connection between two mesh nodes.

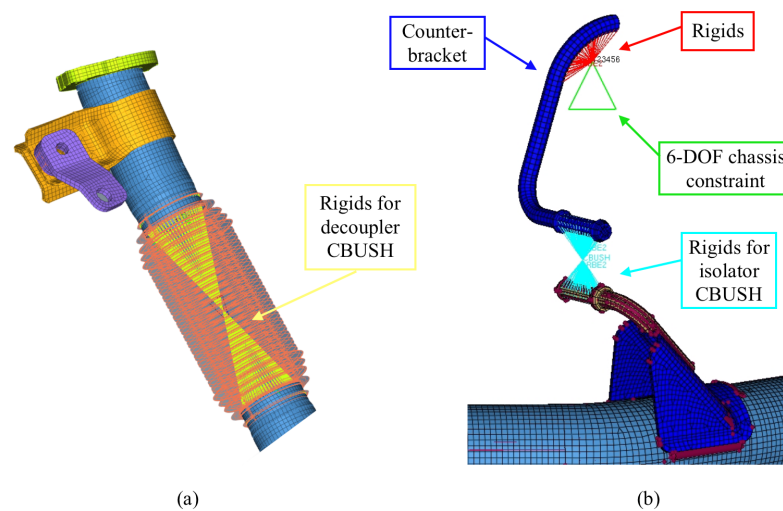


Figure 2.3: Detail of the application of Rigids and CBUSH elements. The flexible decoupler is visible in Figure (a), while a rubber isolators and the connection between counter-bracket and chassis in Figure (b). The CBUSH resides at the intersection of the convergent rigids lines

For the purpose of the structural analysis, any kind of catalytic monolith or filter present in the line accounts exclusively as an additional mass, thus it is unnecessary to model its complex internal structure. Furthermore, since the monolith's material is normally ceramic-based¹, not suited to withstand external loads, its actual presence does not improve the structural properties of the line. In accordance with this principle, whenever the Cold-End incorporates a catalyst or a filter, its modelling is made employing a non-structural² shell with negligible thickness, to which the whole monolith mass is assigned.

¹For particular applications, mainly for closed-coupled pre-converters or for motorbikes, the substrate can be made by a metallic foil shaped in a sinusoidal manner, as depicted in Figure 2.4.

²In FEA, non-structural property indicates the inability of the element to sustain mechanical stresses.



Figure 2.4: *Internal structure on converters substrates: the thin ceramic walls or metallic foil are not suitable to withstand mechanical stresses*

Even if this last sentence might appear inconsistent with the description developed in Section 1.1, it could happen that some Cold-Ends, as it occurred in two of the models analysed, are equipped with converters. Historically, it has been evidenced that this fact occurs immediately after the introduction of a new technology of emission reduction. The first three-way catalytic converters were located in an underfloor position. As the time passed, the catalyst approached the engine outlet ports, up to reaching the so-called close-coupled position, to better exploit the thermal energy of the burnt gas and reduce its light-off period.

This two-step introduction process is the natural consequence of two concomitant factors:

- the necessity of endowing the new produced cars with the incoming technology, to comply with new regulation standards, thus to be allowed to sell the vehicle;
- the impossibility of a sudden modification of the design and production of highly complex components, like the Hot-Ends, which would require a whole re-arrangement of engine bay space.

At present, a similar process is occurring with the Diesel Selective Catalytic Reduction strategy introduction: fitting the SCR directly in the engine compartment, or close to already present elements, like the DPF, is not straightforward. The SCR of models already in production is placed in the under-body, thus it is unavoidably integrated in the Cold-End subgroup. In Section 3.2.1, the countermeasures required to address this problem during experimental tests on the Cold-End will be illustrated.

Further to the definition of the material properties, the FEA requires also an identification of the boundary conditions. At this stage of the analysis,

they principally correspond to the physical constraints to which the counter-brackets are anchored: since no chassis is modelled, it is sufficient to block all the degrees of freedom of the nodes at the interface with the under-body to obtain reliable results.

2.2 Damage evaluation: Road Load Simulation

As mentioned at the beginning of this Chapter, computational fatigue damage estimation in exhaust hanger brackets is achieved comparing local stresses to the relative material fatigue limits, obtained from the Haigh diagram.

To identify the coordinates of the working point for each node in such a plot, it is necessary to discern the overall mechanical stress level into its two components:

- Mean stress (σ_m), caused by the presence of a static load;
- Alternating stress (σ_a), consequence of the application of a dynamic load;

as depicted in Figure 2.5.

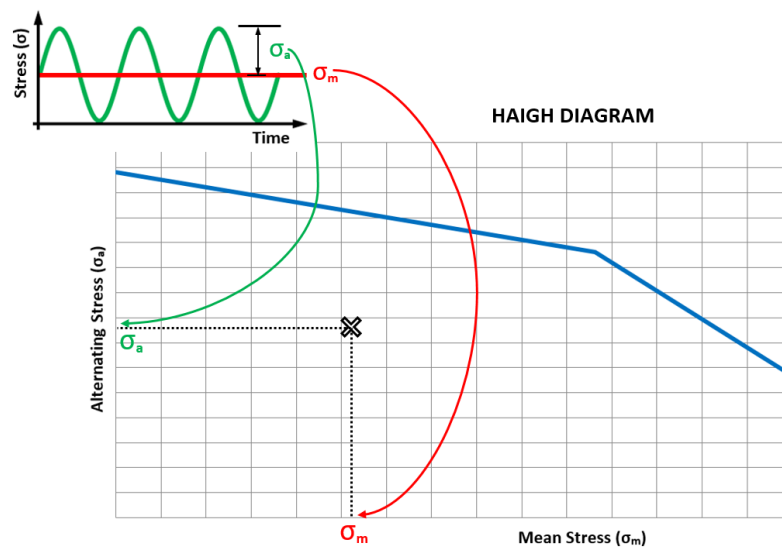


Figure 2.5: *The coordinates of the working point in the Haigh diagram are the static and alternating components of the applied load*

For the validation of hanger brackets, the common practice lead, on one hand, to select as static load the gravitational acceleration, thus the weight of the line. On the other hand, for what concerns the alternating stress value, it has been selected *de facto* the one produced by the **static** application of an analogous acceleration, but with a magnitude of $4g$, i.e. four times the static load. This state-of-the-art approximation had to be applied because the simulation of a real load time history, applying as inputs the data gathered during

the Road Load Data Acquisition (RLDA) on the Proving Ground, is extremely time-consuming and could not be afforded. Indeed, it is worth to remark that, although $4g$ represents an average fictitious alternating excitation, its value, repeated for 500 000 cycles, tends to generate a condition more onerous with regard to the physical driving test, hence this process, being extremely conservative, lead to the production of highly reliable components.

Subsequently, a Safety Factor is assigned to each node of the meshed structure. Its value is computed, according to Equation 2.1, as the ratio between the material fatigue limit and the actual stress of the element.

$$SF = \frac{\sigma_{lim}}{\sigma_{wp}} \quad (2.1)$$

This procedure can be outlined in geometrical terms looking at the Haigh diagram of Figure 2.6. Once the local working point coordinates (namely mean and alternating components) have been located, the corresponding stress level is represented by the segment joining that point to the origin. In a similar manner, the fatigue limit corresponds to the extension of said line until the intersection with Haigh curve.

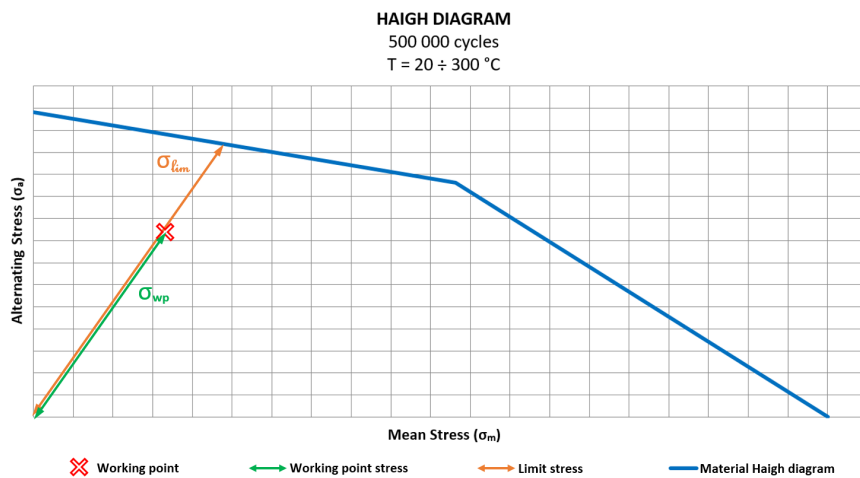


Figure 2.6: The Safety Factor is defined as the ratio between the limit stress (orange segment length) and the local stress (green segment length)

As one can immediately deduce, all the area underneath the Haigh curve represents a zone for which the Safety Factor is larger than unity, whilst, above the curve, the local stress exceeds its limit ($SF < 1$). Whether an operation point falls in proximity of the limit curve, still remaining below it, the Safety Factor approaches unity and an alert should be declared: the component is in a borderline condition.

The Haigh diagram to which the stresses are compared is evaluated at 500 000 cycles, in accordance with customer requests. For the nodes embedded in a weld bead and in the heat affected zone adjacent to it, the values of the Haigh diagram are halved. Even this hypothesis derives from the common practice, therefore its validity should be verified through fatigue tests on specimens. Nonetheless, the adoption of this guideline allowed to produce compliant parts.

When dealing with fatigue, it is also important to consider the working temperature of the material in order to select the proper diagram: higher temperatures reduce the material resistance, as evidenced in Figure 2.7.

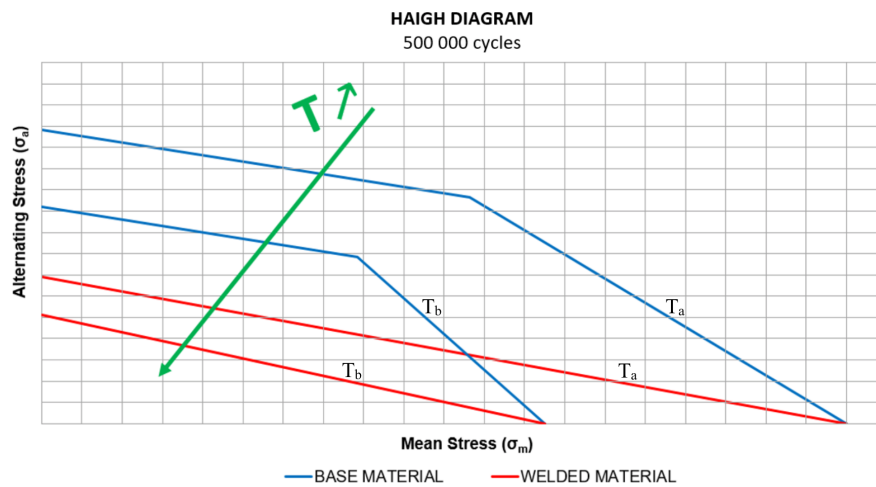


Figure 2.7: Comparison between the Haigh diagram of a base metal and its corresponding welded area at different temperatures ($T_b > T_a$) in linear plot

The outcomes of the simulation are the stress levels in each node of the mesh. Using a post-processor, such as PATRAN, it is possible to visualize the stresses in a Map form, meaning with a chromatic scale on the virtual model itself, as reported in Figure 2.8 condition (a). Despite this is a conventional output of the analysis, it is not immediate to check whether the stress exceeds or not the Haigh limit, especially if the model includes welded elements. To overcome this issue, the Company has developed an internal software for the virtual damage evaluation, which is aimed at producing a Safety Factor Map, like the one reported in Figure 2.8 condition (b). The programme automatically selects the correct Haigh diagram to gauge the local stress level: node by node, it calculates the Safety Factor, applying Equation 2.1, and it assigns its value to the element. Using again a post-processing software, it is possible to re-build the physical model, upon which the Safety Factor Map is shown.

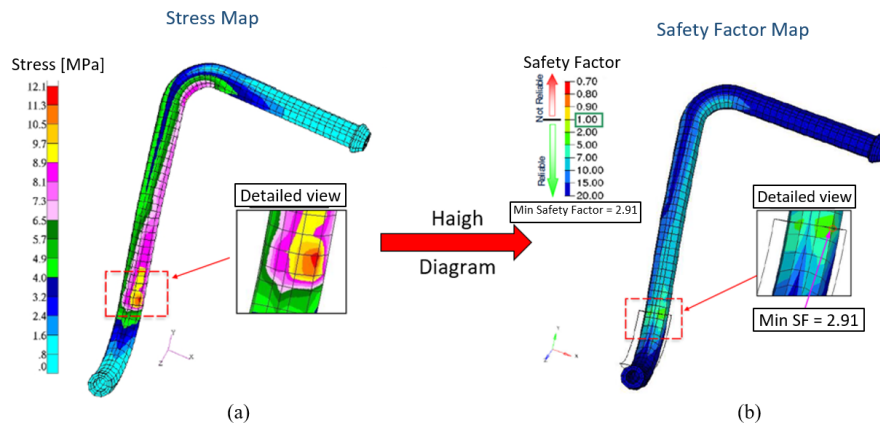


Figure 2.8: *Stress map (a) and corresponding Safety Factor map (b) of an exhaust hanger bracket, obtained comparing the stresses of the first map with the corresponding Haigh diagram*

Courtesy of this adjustment, it is straightforward to identify the most fragile point of the structure. In fact, there is no guarantee that the most stressed point is also the weakest: since the heat affected zones of a weld bead have a lower resistance, a lower stress on them might push the material closer to the limit than a higher stress on the base material. If any zone would result out of target, namely if its Safety Factor is lower than one ($SF < 1$), proper corrective actions, in terms of material or design modifications, can be adopted and their effectiveness assessed repeating the analysis; alternatively, the line is declared valid.

Chapter 3

Experimental validation

The Experimental validation consists of a set of physical tests performed on existing specimens, carried both in the testing facilities and on some specific Proving Grounds, indicated by the customer. The investigation is aimed at assessing if the requirements stated in Section 1.1 are achieved by the real produced components, and eventually at alerting the design department of the mismatch, possibly before mass production starts up.

The principal examinations carried by the testing department are:

- Material, Weight, Leakage and Dimensional checks. The first three are carried mainly on the components, while the last inspection is also aimed at verifying that the critical clearances among under-body components and exhaust line are respected when this last is fitted underneath the vehicle;
- Flow distribution, on a fluid-dynamic bench endowed with Pitot tubes, to ascertain the prediction made during the Virtual simulation about the homogeneous diffusion of burnt gas over converters surface (see Figure 1.2);
- Back-pressure measurement to assess the throttling effect caused by the real exhaust system;
- Thermal shock and Hot Vibration tests, especially for the Hot-Ends, to guarantee infinite thermal fatigue life of these components;
- Shell and Tailpipe noise level evaluation, before and after ageing, to certify the actual produced noise and its durability over time;
- Time to dry, typically for Cold-End members, to avoid water stagnation and potential corrosion of them;

- Physical modal analysis on the Hot-Ends, on hanger brackets, on body counter-brackets and on heat shields, to identify their real modal displacement and to ensure that the first eigenfrequencies lay out of their relative excitation range;
- Mechanical fatigue of hanger and body brackets and of welded junctions between pipes and mufflers, employing the methodologies described in the following paragraphs, to validate their structural resistance when subjected to determined loads and road profiles.

For what concerns the last point mentioned, the predominant requisite of hanger brackets and welded joints is their endurance over the entire vehicle service life: mechanical fatigue is thus the focus of the investigations made on these components. The assessment procedure is based on three pillars:

1. Fatigue test and Wöhler's curve computation;
2. Data acquisition on the Proving Ground;
3. Data analysis and comparison with Wöhler's curve.

3.1 Fatigue test and Wöhler's curve computation

The purpose of this preliminary phase is to determine the mechanical fatigue strength of exhaust hanger brackets and to obtain the component's experimental Wöhler fatigue curve, to which the results of the following steps will be referred. This assay is entirely carried out in the testing facilities, on devoted benches.

To determine the fatigue behaviour of the components, fatigue tests are performed on 10 to 15 physical specimens. The unit under investigation is anchored to the bench, using suitable constraints, in the same position of the one assumed under the vehicle. Then, a symmetrical sinusoidal load, characterized by determined amplitude F and frequency f as illustrated in Figure 3.1, is applied.

Conventionally, the load is applied by hydraulic jacks along the most critical direction highlighted during the RLDA (Road Load Data Acquisition) or, in absence of such an information, according to previous knowledge and experience it has been evidenced that vertical (Z) direction is the most severe. Occasionally, if the customer declares it explicitly, other orientations may be adopted.

Different loads are applied to each specimen to thoroughly explore the Wöhler's plot. If data of RLDA are available, the level of the first load is the maximum measured during the driving test on the specific component. On

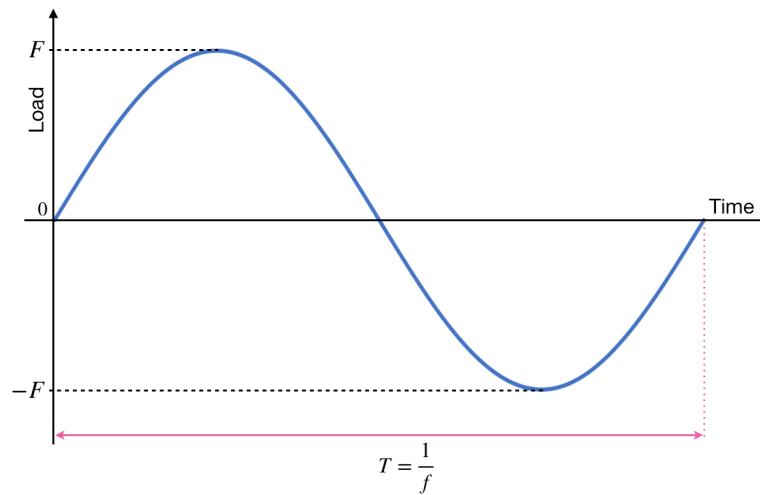


Figure 3.1: *Sinusoidal symmetric load applied during the fatigue characterization*

the contrary, if the aforementioned data have not been gathered yet, its value is tuned on trials made on two exploration samples, also considering prior experience on comparable parts.

The test is carried under load control: the force entity is monitored by a load cell placed between the hydraulic jack extremity and the test item, as displayed in Figure 3.2: a feedback control exploits this signal to adapt the push-rod stroke in order to maintain the force within the 5% of the value set by the operator (peak/valley compensation control).



Figure 3.2: *Hydraulic jack employed for fatigue characterization: the black element at the rod tip is the load transducer*

Once every parameter has been specified, the test is launched. The rod, pulsating at a frequency within $5 \div 20$ Hz, stresses alternatively the bracket engendering a purely fatigue damage. The system increments the value stored in a counter whenever a cycle has been completed.

Since the applied load is kept constant by the controller during each repetition, an increase in stroke of the hydraulic jack suggests that the sample is weakening. As the rod displacement exceeds 150% of the initial one, devoted alerts are triggered and the test is concluded. A visual inspection, even with penetrating liquids if required, is mandatory to ascertain that the part presents effectively a crack. In such circumstances, the number of cumulated load cycles is recorded, along with the value of the load applied, otherwise, if no fracture occurred, the sample is considered broken at 2 million cycles.

The obtained experimental values are plotted on a bi-logarithmic diagram, whose abscissa axis indicates the number of cycles whilst the ordinary axis reports the load applied, and, after their interpolation, the Wöhler's curve of the particular feature is obtained. The regression line that describes the component's fatigue behaviour is linear in the logarithmic plot and is represented by the Equation 3.1.

$$\log_{10}(N) = A + B \cdot \log_{10}(S) \quad (3.1)$$

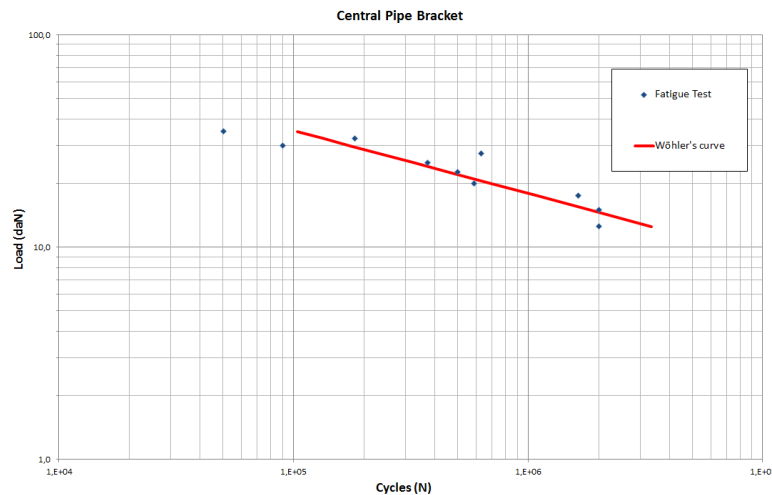


Figure 3.3: *Example of a Wöhler's curve of an exhaust bracket obtained interpolating the results of the fatigue test on a physical component*

It would be also possible to obtain plots containing probability curves, which have been computed according to the *ASTM E739-10* international norm, to obtain a curve more significant for the entire production.

3.2 Data acquisition on the Proving Ground

The purpose of this activity is to acquire data relative to the dynamic loads to which the exhaust line is subjected during standardized operating conditions, to be compared with the previously defined Wöhler's fatigue curves. To attain this objective, the vehicle involved in the investigation is equipped with a

dedicated exhaust system, upon which some sensors have been installed, and it is driven on specific a Proving Ground, established in accordance with the customer. During this phase, a Data Acquisition system (DAQ) samples and records data. An individual acquisition batch is dedicated to each specific track: the segmentation of the whole test time history, further to shortening the trial run, allows to understand which is the most severe pavement/condition and to obtain the overall cumulative by multiplying the contribution of each track by its relative weighting factor: further details of these procedures are presented in the next Sections.

3.2.1 Test exhaust line preparation

Gas Deviation As mentioned in Section 1.1, the Cold-End of an exhaust system has to bear principally mechanical loads, because the thermal effect has a negligible impact. In order to evaluate exclusively mechanical solicitations on the line, it is necessary to bypass the hot exhaust gases immediately downstream the close-coupled catalytic converter(s), possibly before the beginning of the Cold-End. This countermeasure is implemented by drilling a hole of suitable diameter in the external surface of the pipe and plugging the duct by welding the removed part immediately upstream the orifice, as shown in Figure 3.4.

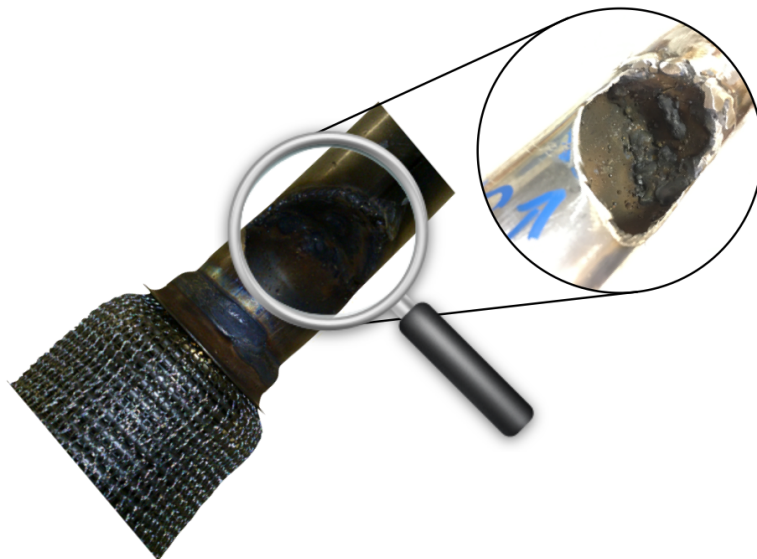


Figure 3.4: *Gas deviation immediately downstream the flexible decoupler, at the beginning of the Cold-End*

In the event that an under-body after-treatment element is integrated in the Cold-End, for the reasons mentioned in Section 2.1, a bypass would impair the operation of the sensors, thus of the entire vehicle, since the ECU (Engine Control Unit) would detect a malfunctioning, lighting on the dashboard a

proper indicator (MIL) or even limiting the engine power (typical countermeasure triggered in case of urea shortage in vehicles endowed with SCR). In this case, as it occurred with one of the models analysed and shown in Figure 3.5, the deviation must be practised downstream the last sensor.

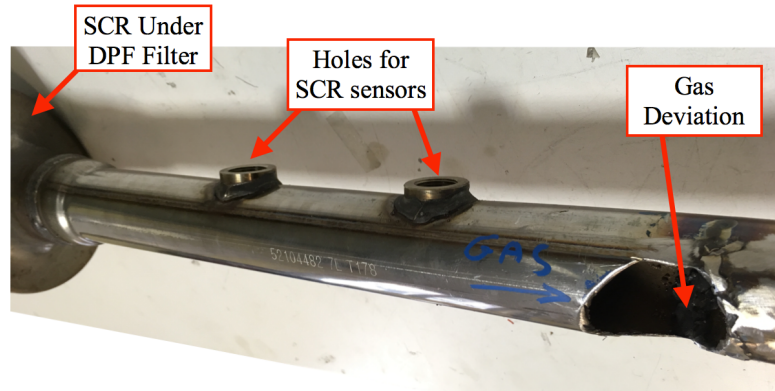


Figure 3.5: Whenever the Cold-End comprises after-treatment devices, the gas deviation must «*aqqqqbe drilled downstream all the related sensors, not to impair vehicle functioning*»

A secondary advantage provided by the bypass of hot gas is that it enables the application of low-temperature strain gauges, which are easier to be applied and have a lower cost with respect to their hot counterpart.

Strain gauges theory The aim of the experimental verification is to acquire the loads acting on hanger brackets and welded joints during the driving test in the same points and directions of the fatigue characterization. These loads are retrieved indirectly from strain measurements on the aforementioned components obtained applying uni-axial, low-temperature strain gauges with a grid length of 2 mm on the specimens, as shown in Figure 3.6.

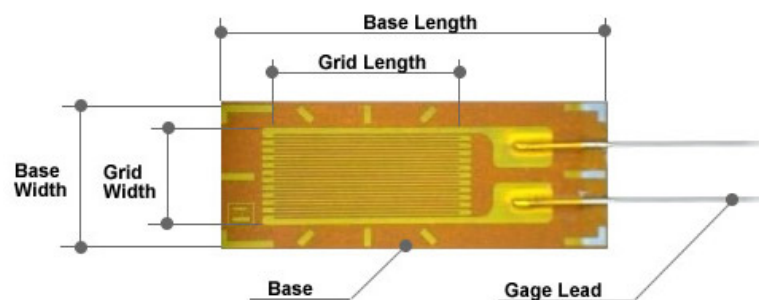


Figure 3.6: Scheme of an uni-axial strain gauge

The working principle of these transducers is based on the variation of electrical resistance of materials when subjected to tensile or compressive forces, according to Equation 3.2:

$$\frac{\Delta R}{R} = K_s \cdot \varepsilon \quad (3.2)$$

where R is the gauge nominal resistance at rest, ΔR is the variation of it, K_s is a gauge factor expressing the sensitivity of the transducer, while ε is the mechanical strain, defined in Equation 3.3, is the relative length variation.

$$\varepsilon = \frac{\Delta l}{l} \quad (3.3)$$

Being the resistance change very modest, a Wheatstone bridge configuration is employed to magnify the variation and to convert it into a voltage change. This routine is normally actuated within the acquisition device, selecting the desired connection type, but it can also be done externally by the operator, as described in the next Paragraph.

Strain gauges positioning Low-temperature strain gauges are applied on metallic specimens using a cyano-acrilate based glue. The transducer is maintained pressed in its position by an adhesive tape until the glue gets dry. At this point, the gauge is able to track the strain of the substrate material.

Conventionally, four gauges are installed along the circumference of the elements, at 90 deg among each other, as depicted in Figure 3.7, to acquire loads along Z and Y (or X) directions. The sensing grid is normal to the action line of the load, whilst it is parallel to the direction of elongation of the hanger.

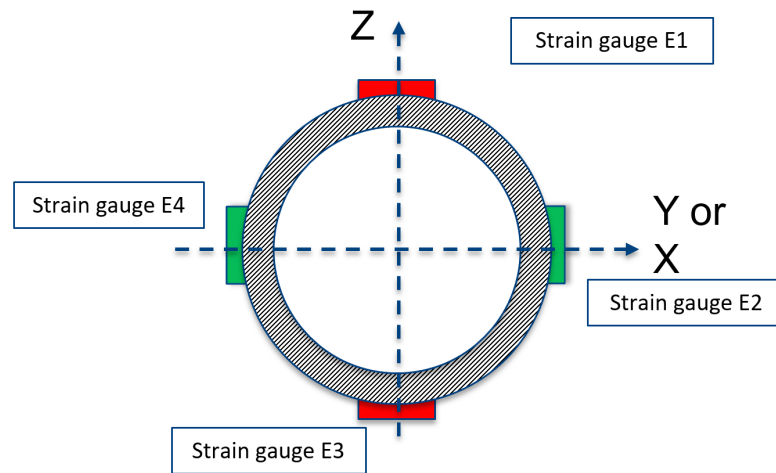


Figure 3.7: Naming convention and relative position of strain gauges on hanger brackets or welded junctions

The strain gauges can be used individually, in a quarter-bridge configuration (Figure 3.8 condition (a)), or connecting two opposite sensing elements (e.g. E1 with E3 and E2 with E4) in a half-bridge topology (same Figure condition (b)).

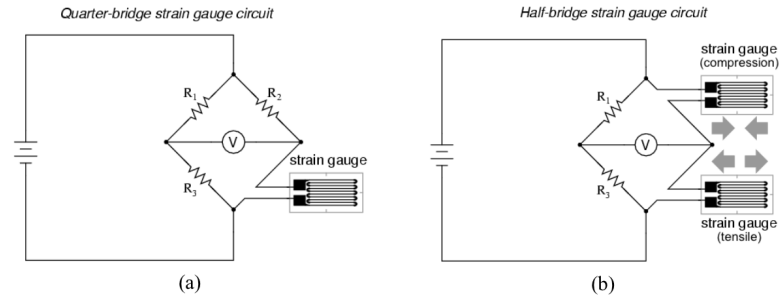


Figure 3.8: Quarter bridge (a) and Half bridge (b) connection layouts

The redundancy provided by the number of sensing elements employed is not mandatory and can be neglected in presence of external constraints, like the lack of available space, but it revealed to be convenient in that:

- the former topology grants the acquisition some data even if one of the two opposite channels is impaired or totally lost (perhaps after mounting operation beneath the vehicle or if the gauge detaches from the base material);
- the same connection offers the possibility of comparing opposite channels readings to check the correctness of acquired data during the post-processing analysis operation (they should be opposite in phase in case of bending load applied to the feature);
- the latter strategy's benefit is the automatic correction of offsets and global trends, since only deformations with opposite values are read and amplified: two strains congruent in amplitude and direction discarded by the electric behaviour of the circuit itself.

For some peculiar application or analysis, also other sensors like thermocouples or rosettes (three uni-axial strain gages forming an angle of 45 deg among them) might be employed: the former are used to sense material temperature, while the latter measure local mechanical stress.

Driving test The vehicle is finally driven on some specific Proving Grounds, according to a procedure established by the customer, in the so-called RLDA test. The tracks are paved with calibrated surfaces aimed at reproducing the vast majority of possible conditions that the exhaust line would encounter during its operating life. Data concerning the brackets strains and stresses (only if rosettes are employed) are recorded per each track, using a specific acquisition instrumentation and a PC. One run over each track is enough to capture the relevant data; a second passage is performed some anomalies are revealed by the operator.

Data from each sensor is sampled at a rate which allows to capture the deformation time histories with a satisfactory resolution.

3.3 Data analysis and comparison with Wöhler's curve

After the physical trial, the acquired strain time histories are corrected and analysed. The main corrections are aimed at the removal of false peaks in the readings, sometimes due to EMI (electro-magnetic interferences) and very likely present at the beginning and at the end of the data recording, at reducing the effect of offset with respect to zero and drift, often due to thermal elongation of hot components, especially if the gas deviation occurs after some gauged element.

At the end of this refining process, the time histories of every single pavement are juxtaposed consecutively, applying a proper multiplication factor to each of them, to obtain a global overall time history. This last would equal, in terms of damage, the repetition of the driving test over each pavement for the aforesaid multiplication coefficient: the advantage of such a procedure is evident. The necessity of the data correction, mentioned at the beginning of this Section, becomes now apparent: if a time history features few very high peaks caused for instance by an interference, the multiplication *tout court* of its data can lead to a misleading overestimation of the damage, perhaps impairing the validation result.

3.3.1 Strain gauges calibration

The instrumented exhaust line is dismantled again from the vehicle and the strain gauges are calibrated in the laboratory, in order to find the relationship between the load applied on the bracket (or junction) in the same position and direction of the fatigue test and the corresponding deformation, measured in μ strain.

$$1 \mu \text{ strain} = \frac{1 \mu\text{m}}{\text{m}} = 10^{-6} [-] \quad (3.4)$$

As done during the fatigue characterization, the exhaust line is oriented and positioned in the same way as underneath the vehicle and rigidly constrained to a fixed reference. Subsequently, some calibrated weights, of one or five kilograms each, depending on the element to be gauged, are applied progressively, using a support, in the same points in which loads are detected during the driving test (Figure 3.9). Both vertical and transversal directions are analysed if strain gages are applied as depicted in Figure 3.7.

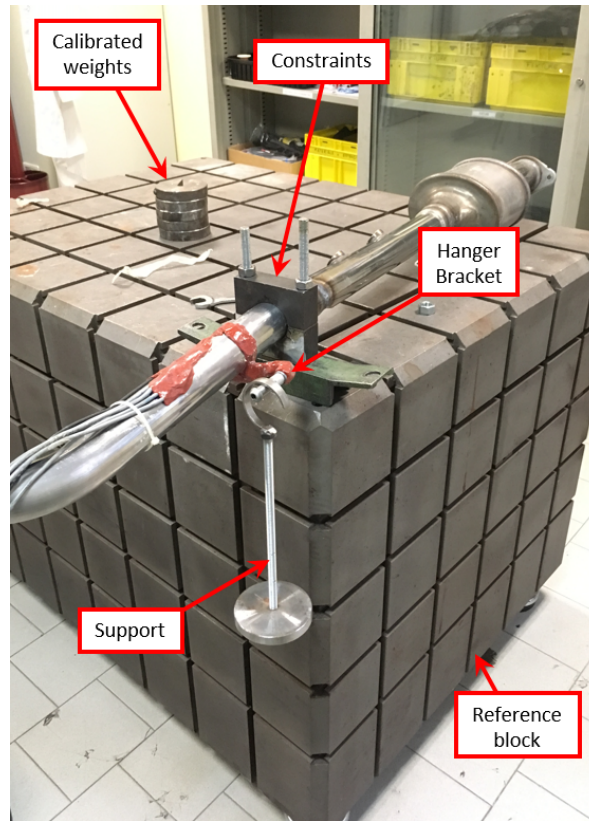


Figure 3.9: *Central pipe hanger calibration: the line is constrained to the reference block and gauged weights are applied progressively on the support. In the same time, the hanger strain is recorded by the acquisition instrument*

Concomitantly, the corresponding strains are recorded, both during the loading and the unloading of the weights, as illustrated in Figure 3.10. Again, this duplication permits a double check between the readings.



Figure 3.10: *Strain time history during the calibration: the symmetry between the loading and unloading phases indicates the correctness of the readings*

From the obtained values of deformation, it is possible to extract the calibration coefficients of each feature (hanger bracket or junction) in the direction sensed by the strain gauges, as explained above. In the following, an example is proposed:

Point 1 (Z direction)	
Load [daN]	Strain [μ strain]
0	0
1	7
2	14
3	21.5

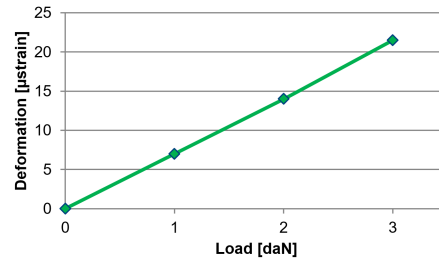


Figure 3.11: *Load-Strain characteristic of an exhaust hanger bracket under calibration*

The slope of the regression line obtained interpolating the experimental points corresponds to the calibration coefficient, which represents the deformation law of the element with respect to the load applied in a specific direction. For the previous example, the coefficient is:

$$\frac{\text{Load}}{\text{Deformation}} = 0.142 \frac{\text{daN}}{\mu \text{strain}}$$

Exploiting the calibration parameters of each bracket and each direction, it is possible to convert the strain time histories gathered from the driving test into load time histories acting in the same direction of the fatigue test (Figure 3.12).

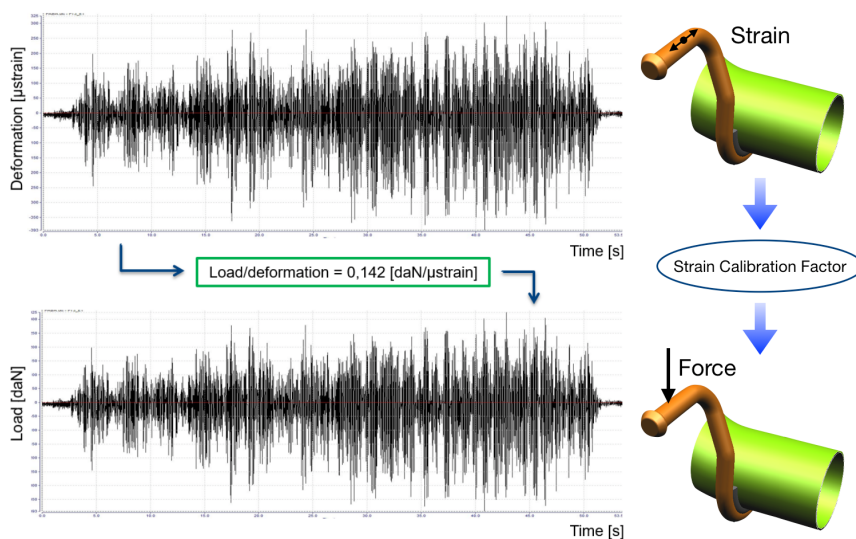


Figure 3.12: *The strain time history of each element (first plot) can be converted into a load time history (last plot) by multiplying each value by the relative calibration coefficient*

3.3.2 Damage evaluation and Validation criterion

The cumulative load count, which is the element to be compared with the Wöhler's curve is obtained applying the Rainflow, sometimes named Waterfall, counting method to the load time history of each pavement. This procedure synthesises in a table and in a graphical manner the number of occurrences of a certain load on every bracket or junction during the RLDA test.

Eventually, the cumulative loads of every single pavement are superimposed, applying to each of them a proper multiplication factor, to obtain a global overall cumulative. This last would equal, in terms of damage, the repetition of the driving test over each pavement for the aforementioned coefficients: the advantage of the computational a procedure is evident. As said, the plot of the global cumulative, namely the Rainflow diagram, can be directly compared to the Wöhler's diagram, as shown in Figure 3.13.

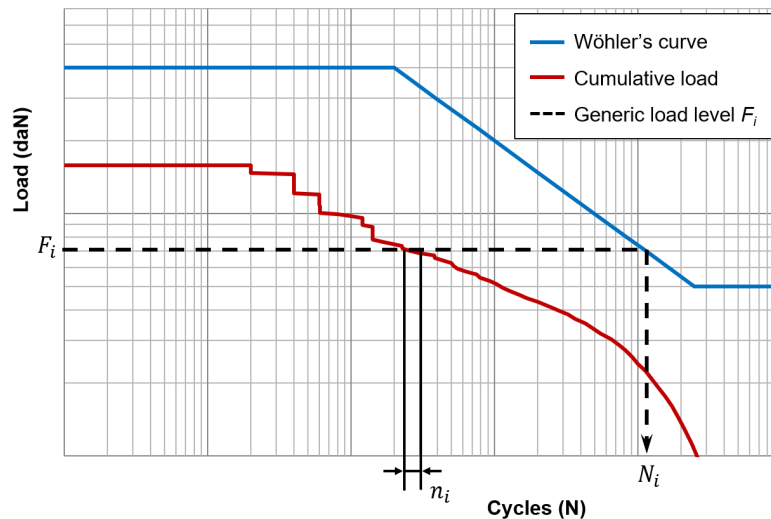


Figure 3.13: Chart of both Wöhler and cumulative curves of a component. In black are evidenced the characteristics necessary for Miner's damage evaluation

As a first approximation, to check whether the component can withstand the target life, it is necessary that the cumulative curve lays completely below the Wöhler's one. Nevertheless, a more robust result is provided by the computation of the cumulated Damage with Miner's rule. According to Miner, each cyclic load causes a damage proportional to its level and to the number of repetitions, provided that the stress exceeds the endurance limit, below which fatigue life is not affected, which is accumulated in the part itself, reducing its residual life.

The damage contribution is evaluated for each load level according to Formula 3.5, starting from the load time history (or cumulative) and Wöhler's

curve of the component.

$$d_i(F_i) = \frac{n_i}{N_i} \quad (3.5)$$

A comparison with Figure 3.13 clarifies the meaning of the terms appearing in the Equation 3.5: the damage contribution d_i caused by the load F_i corresponds to the ratio between the actual number n_i of occurrences of that force and the maximum number of repetitions N_i of the same load that would lead the component to fatigue failure. The sum of all these ratios provides the Damage caused by the specific cumulative, as highlighted in Formula 3.6.

$$D = \sum_{i=1}^{i_{tot}} \frac{n_i}{N_i} = \sum_{i=1}^{i_{tot}} d_i \quad (3.6)$$

The component undergoes fatigue failure once the accumulated damage reaches the value of 1.

The necessity of the data correction, mentioned in Section 3.3, becomes now apparent: if a time history features few very high peaks caused for instance by an electro-magnetic interference, the multiplication *tout court* of its data can lead to a misleading overestimation of the damage, perhaps impairing the validation result.

Validation condition At the end of this procedure, the component is deemed validated by the Testing department whenever the Experimental Safety Factor, computed on the basis of strain gauges acquisitions and defined as the inverse of the damage, exceeds the value of 1.2.

$$SF_{experim} = \frac{1}{D} \geq 1.2 \quad (3.7)$$

Chapter 4

Equivalent load

4.1 Differences between the methods

The previous Chapters already highlighted the discrepancies that exist between the two validation methods ordinarily employed.

First of all, the two procedures start from different inputs: while experimental tests are carried with a real vehicle on different Proving Grounds, thus the solicitations on the exhaust system that result are thoroughly dynamic, virtual validation applies only static loads, even to represent a dynamic condition (remember the assumption made in Section 2.2 selecting as alternating stress σ_a the upshot of the application of a static load).

With this simplification, the effect of time-evolving accelerations cannot be appraised.

Moreover, the outcomes of the analyses are not directly related each other. From the physical data acquisition, the cumulative load (in kg) acting on each bracket and the relative damage are obtained using Wöhler's curve of the component and Miner's rule. On the other hand, the natural result of the computer simulation is a Stress map (whose values are in MPa), at the utmost converted into a Safety Factor map, with values referred to 500 000 cycles, using the Haigh diagram of the material.

Section 3.3.2 points up a further dissonance that exists between the procedures: the results are referred to different fatigue curves and technically they cannot be compared as such. While the experimental analysis identifies the proper Wöhler's curve for each component, measured in [kg/cycles], through the fatigue bench characterization, the virtual simulation relies on Haigh diagrams of the material, expressed in [MPa/cycles]. The latter differs from the former in that it neglects the effect of the actual geometry.

In Table 4.1 the analysed differences existing between virtual and experimental validation methods are summarized.

	Virtual	Experimental
Input	1 g + 4 g	Proving Ground
	Static	Dynamic
Output	Stress map [MPa]	Brackets cumulative load [kg]
	Safety Factor map	Damage (with Miner)
Fatigue test	Haigh diagram of material and weld beads	Component's Wöhler's curve

Table 4.1: *Summary of the differences between the validating methods*

4.1.1 Correlation proposals

To overcome the limitations highlighted in the previous Section, multiple alternatives have been discussed to determine their appropriateness. In the following will be explained some solutions that have been proposed and attempted in order to reduce such discrepancies.

4.2 Equivalent load

The first correlation technique is an heuristic procedure that attempts to abate the differences, in terms of fatigue reference curves, that exist between Virtual and Experimental validation methods, as highlighted in the last row of Table 4.1. Considering that the Haigh diagram, to whom mechanical stresses are compared for the computation of the Computed Safety Factor, is evaluated at 500 000 cycles, this methodology strives to identify a static load which, applied 500 000 times, is equivalent, in terms of damage, to the cumulative load deriving from the Proving Ground experimental test.

Eventually, the new results are compared to the conventional 4g procedure with the expectation of finding a clear and repeatable relation between the outcomes, ideally a corrective coefficient, to obtain more correlated results.

The details of the methodology, along with the required data and the outcomes of the comparison will be described in the following.

4.2.1 Objective

The basic purpose of the equivalent load computation is to reduce the whole load time history (thus the load cumulative), deriving from RLDA data acquisition, to a single force level which produces the same damage of the driving test if applied for a specified number of repetitions. Therefore, an equivalent force will be defined for each single component of the exhaust line for which deformation data and Wöhler's curve have been acquired. In the present study, only exhaust hanger brackets have been analysed.

More in depth, the objective is to verify whether the application of these loads on their relative brackets produces stresses comparable to the tradi-

tional 4g validating test and eventually, whether a clear trend could be found, to assess the relation existing between them.

4.3 Input data

For each element analysed, being it a hanger bracket or a welded junction, the data required as input for the evaluation of equivalent loads are:

- Wöhler's curve (Equation 3.1), in particular its coefficients A and B , obtained from the experimental characterization at the hydraulic jacks (Section 3.1);
- Cumulative of loads, namely a table containing number of occurrences n_i of a determined load F_i , recorded during the RLDA acquisition.

The cumulative is obtained applying the Rainflow counting method to the complete time history of the driving test. A dedicated software scans the acquisitions and extracts the number of cycles corresponding to a certain load (or strain, since they are proportional) range. In practice, when a cycle is identified, the related entry of the Rainflow matrix is incremented: in this way, each element of the matrix expresses the number of cycles, evidenced in the time history, corresponding to each range. The two cycles represented in Figure 4.1, equal in amplitude and differing only for the extreme values of the range, would be accounted for in different entries of the matrix.

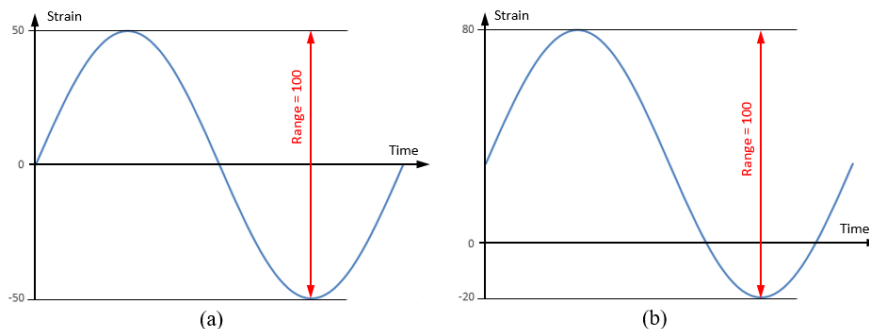


Figure 4.1: *Two strain (or load) cycles with the same range but different extrema would be registered in different strain (or load) batches*

In the peculiar case of the driving test, since the exhaust line oscillates about its rest position and the boundary conditions to which it is subjected are unchanged at the end of the test with respect to the initial ones, there is no specific reason to have cycles with a non-zero mean value. Pursuant to this consideration, for the evaluation of the equivalent load, only the amplitude ranges are considered. Although this simplification would underestimate the fatigue damage, because the effect of mean stress is not taken into account, the

error introduced is not impacting for the purpose of the analysis, being minimal the unbalance with respect to the origin. By virtue of this consideration, in this study, the two cycles of Figure 4.1 would be considered equivalent in terms of fatigue damage.

4.4 Computation

The calculation of the Equivalent load commences with the estimation of the damage generated by the repetition (n_i times) of each load F_i exploiting again Miner's rule (as explained in Section 3.3.2). Then, summing all the individual contributions, the overall damage on the component, relative to the load time history is obtained:

$$D = \sum_{i=1}^{i_{tot}} d_i = \sum_{i=1}^{i_{tot}} \frac{n_i}{N_i} . \quad (3.6)$$

Reached this point, the objective is to identify the unique load level F_{eq} that, replicated for an arbitrarily number n_{eq} of times, engenders on the structure the same overall damage of the original time history. According to Miner, this coincides to state that the ratio between the equivalent number of cycles n_{eq} and its relative fatigue limit N_{eq} must equal the aforementioned damage. Translated in formulas, this statement becomes (Equation 4.1):

$$D = \sum_{i=1}^{i_{tot}} \frac{n_i}{N_i} = \frac{n_{eq}}{N_{eq}} . \quad (4.1)$$

Inverting Equation 4.1, one gets the unknown N_{eq} (Equation 4.2):

$$N_{eq} = \frac{n_{eq}}{D} . \quad (4.2)$$

Substituting this last value in the Wöhler's equation (Equation 3.1), and inverting the formula, the desired equivalent force F_{eq} is obtained.

$$\log_{10}(F_{eq}) = \frac{\log_{10}(N_{eq}) - A}{B} \quad (4.3)$$

The procedures described in this paragraph are synthesized and expressed in a graphical manner in Figure 4.2.

It is worth to remark that the value n_{eq} of cycles is a parameter which, by its nature, can be imposed in accordance with the objectives to be pursued: in the presented analysis, the value of $n_{eq} = 500\,000$ cycles has been selected to match with material characterization (Haigh diagram) employed for the evaluation of the virtual Safety Factor.

ϵ [μ strain]	F_i [daN]	n_i [cycles]	N_i [cycles]	d_i [-]
151	8.02	54	95 136.3	0.0117
133	7.05	249	181 520.5	0.0061
129	6.89	614	203 904.8	0.0030
114	6.07	1725	381 225 .2	0.0045
\vdots	\vdots	\vdots	\vdots	\vdots
52	2.76	17 984	19 912 580.9	0.009
44	2.35	27 836	44 109 501.4	0.0006
38	2.03	39 479	92 645 023.2	0.0004
\vdots	\vdots	\vdots	\vdots	\vdots

Table 4.2: Table for the computation of Equivalent loads: F_i is obtained multiplying half strain range by the calibration coefficient $\frac{\text{daN}}{\mu\text{strain}}$. N_i and d_i have been computed using Wöhler's (3.1) and Miner's (3.6) Equations respectively

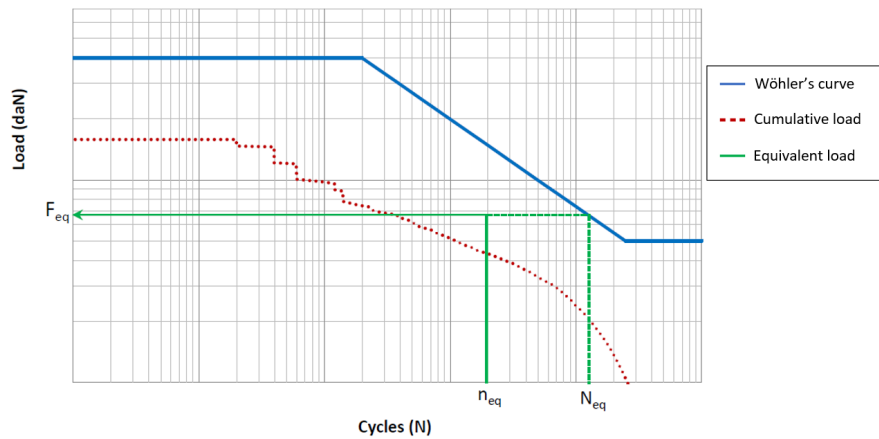


Figure 4.2: Graphical representation of the evaluation of the equivalent load: the ordinate of the intersection between the Wöhler's curve and the vertical line passing from N_{eq} corresponds to the equivalent load

4.5 Results comparison

There exist two possible alternatives to assess the differences between the results of the two methods (4g and equivalent loads):

1. **Load comparison:** compare the equivalent load acting on the bracket to the force which, applied in the central point of the bracket, generates the same stress of the 4g static acceleration. In order to deduce such a force, it is mandatory to retrieve the relation between the simulated stress produced and the force applied virtually on the bracket, which will be called *virtual calibration* and explained in its details in Section 4.5.1;
2. **Stress comparison** run a second virtual simulation, having as inputs the equivalent loads on each bracket, and check the stresses in homologous nodes on the structure.

Although both strategies have been experimented, the results will be proposed according to the former methodology, while the latter will cover an ancillary function and will be quoted for completeness.

As mentioned, to collate the two methods it is necessary to identify some common parameters: in this case-study, bracket loads will be selected as objects of the comparison. The virtual validation analysis provides a stress map, consequence of the application of $4g$ gravity acceleration. It is possible to translate the stress level obtained into the load applied at the bracket involving a numerical calibration coefficient: this factor expresses the relation between force applied in the centre of the bracket and stress of a node, in the same manner in which the stiffness of a spring relates its deformation to the force applied at its extremities. Obviously, while in the spring case the axial deformation is a global property, unambiguously determined, for what concerns stress calibration factor it is necessary to estimate in both conditions the stress in the same node, since the relation is tailored on it.

4.5.1 Virtual calibration

The virtual calibration is aimed at obtaining a relation between the load applied on the bracket and the resultant stress generated on the bracket. This factor can be easily evaluated by making the ratio between the stress level in a specific node and the load applied on the single bracket.

$$\text{Calibration Factor} = \frac{\text{Stress}}{\text{Applied load}} \quad (4.4)$$

Each bracket is isolated from the others by constraining all the circumferential nodes of the pipe upstream and downstream the feature, as highlighted with green rectangles in Figure 4.3, and a predefined load is applied in

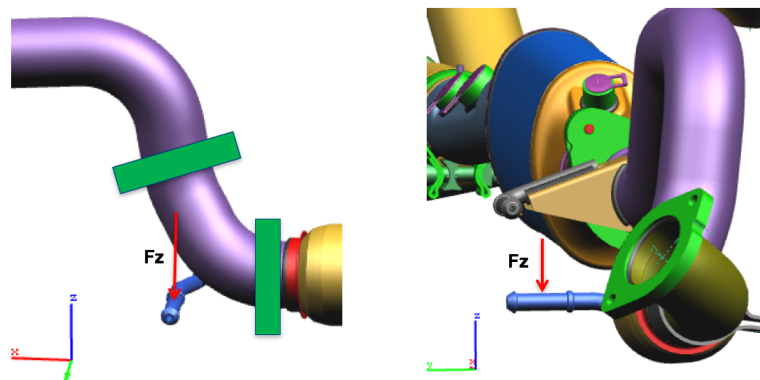


Figure 4.3: *Virtual calibration load and constraint conditions: green rectangles indicate the location of the 6-DOFs constraints, while a predefined load is applied on the centre of the bracket straight portion*

the centre of the bracket, along the negative vertical direction. From the stress map obtained, a node will be selected and exploited for the computation of the calibration coefficient.

Owing to the analogy between static simulation and experimental test, in terms of calibrations, it is possible to assess the differences existing between the methods, given the same boundary conditions, thus to indirectly estimate the error band that affects the results. During the investigation, both virtual and experimental calibrations have been acquired and compared each other.

In the same way, in the testing facility, the brackets are characterized experimentally applying similar constraints and forces, as demonstrated in Figure 4.4. The redundancy of fixtures has been adopted to clone the boundary

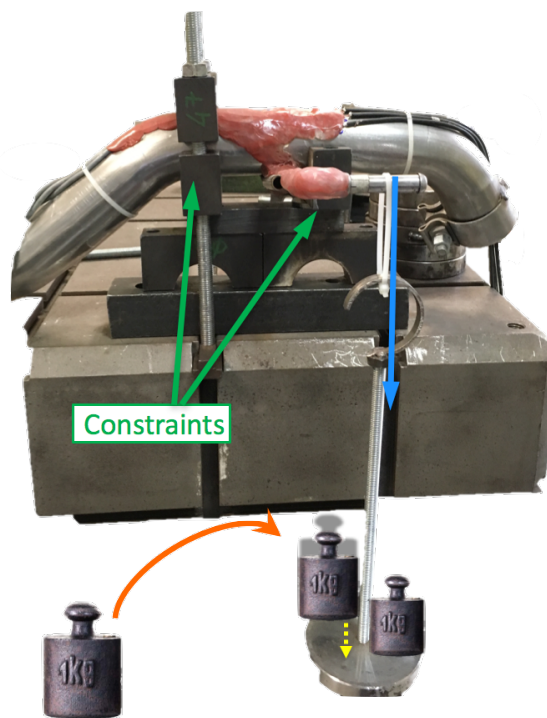


Figure 4.4: *Experimental calibration for the stress coefficient. In the specific case, the constraint conditions of the virtual case have been reproduced to assess also the quality of the simulation*

conditions of the virtual test: reducing such differences, it is possible to assess the correlation between the two experiments.

For the purpose of obtaining a better comparison, further to uni-axial strain gauges placed in the positions indicated in Figure 3.7, brackets have been equipped with Rosettes: these are particular deformation transducers, composed of three superposed uni-axial strain gauges inclined among each other, which allow to measure the mechanical stress.

To assess the distance between the two methods, it is fundamental to compare the outcomes of the virtual calibration in homologous points: the reading

of the mesh node corresponding to the point of application of the rosette must be selected as shown in Figure 4.5. Said difference has been evaluated according to the convention expressed in Equation 4.5:

$$\Delta\% = \frac{\text{Experimental} - \text{Virtual}}{\text{Virtual}} \quad (4.5)$$

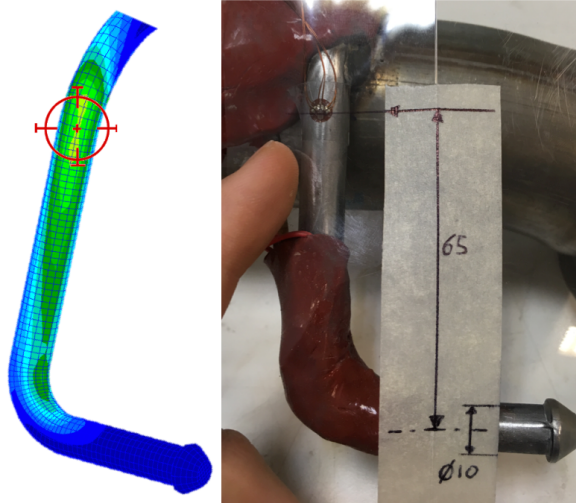


Figure 4.5: To reduce the inaccuracy, it is fundamental that the stress obtained with the two calibrations has been measured in the same point

Despite the efforts in the identification of the exact gauged point counterpart, and also because of the approximations in the stress values, the introduction of errors is unavoidable and, for this reason, must be taken into account.

All in all, looking at the results proposed in Table 4.3 and considering the limitations of the investigation, it can be stated that the correlation between virtual simulation and experimental test results, in static conditions, is satisfactory.

520 - No muffler

	Stress/Load [MPa/daN]		
	Exper.	Virt.	$\Delta\%$
PT A	5.40	5.45	-0.9 %
PT B	4.53	4.79	-5.5 %
PT C	4.44	4.21	5.5 %
PT D	4.12	3.29	11.6 %

(a)

356

	Stress/Load [MPa/daN]		
	Exper.	Virt.	$\Delta\%$
PT A	5.38	5.80	-7.2 %
PT B	5.51	4.37	26.2 %
PT C	5.54	6.13	-9.7 %
PT D	7.85	7.14	9.9 %

(b)

Table 4.3: Comparison between stress calibration coefficients in homologous points: the modest difference ($\Delta\%$) is principally attributable to the error in the individuation of exactly corresponding nodes

For completeness, in Appendix A also the strain calibration coefficients of the same models are reported.

4.5.2 Computation of the brackets loads

Once the calibration factors are available, one can obtain the load acting on the bracket multiplying it by the stress in the same node employed for the calibration: a schematic of this procedure has been composed in Figure 4.6. All these passages have been repeated for several models: some results are proposed in the Tables 4.4.

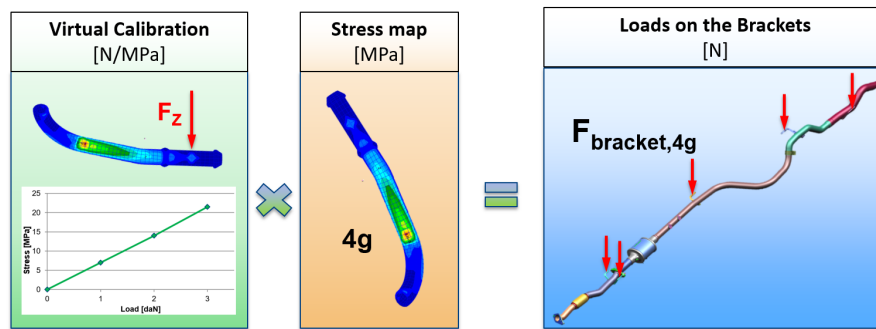


Figure 4.6: Scheme of the procedure followed to compute brackets loads starting from the stress map of the feature and the calibration factor

520 - No muffler				356			
	Brackets Load [daN]				Brackets Load [daN]		
	Equiv.	4g	$\Delta\%$		Equiv.	4g	$\Delta\%$
PT A	7.3	10.5	-30 %	PT A	5.54	5.45	1.5 %
PT B	10.8	13.6	-21 %	PT B	4.94	8.96	-45 %
PT C	8.0	6.7	20 %	PT C	3.26	3.96	-18 %
PT D	6.7	8.4	-20 %	PT D	2.98	4.87	-39 %

(a) (b)

Table 4.4: Comparison between Equivalent loads (experimental) and brackets forces corresponding to 4g procedure (virtual results). The absence of a clear trend between the results highlights the inadequacy of the method

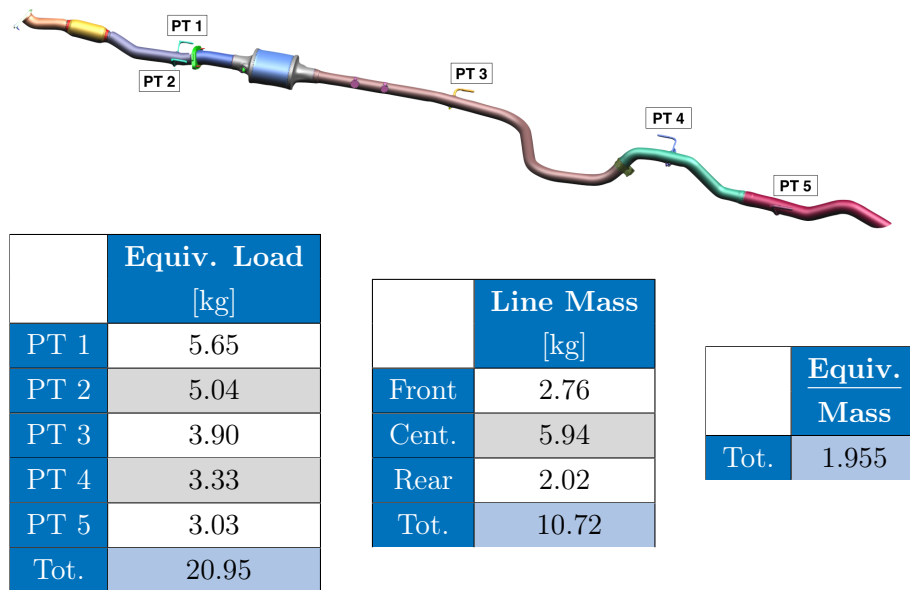
4.6 Comment and critical issues

Undefined trend Despite the expectations, the Equivalent load method revealed unsuitable for reducing the gap between the validation methods. In fact, albeit minor differences between the calibration coefficients have been

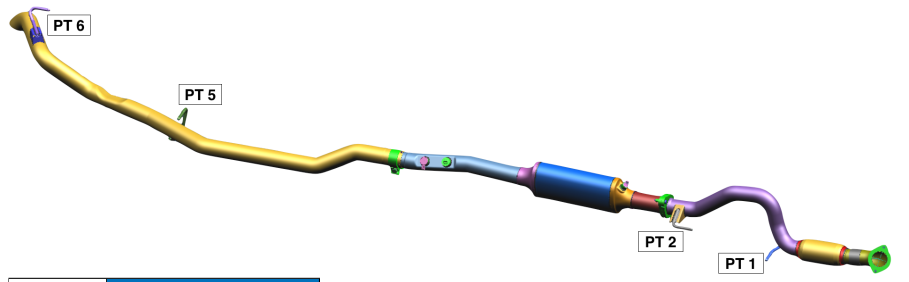
detected, principally ascribable to a lack of precision of the method proposed in Section 4.5.1, the non-existence of an univocal trend between the results of equivalent loads and customary $4g$ validation, in terms of bracket forces, indicates the absence of correlation between the methods. Therefore, in these circumstances, the innovative procedure cannot be adopted as approval method in place of the conventional practice, since in general the equivalent loads reveal to be more severe than $4g$ ones.

Influence of the layout A supplemental finding, discovered along the analysis of the equivalent loads of different exhaust systems, evidences the strict dependence of these forces on the line layout.

The scrutiny was aimed at unveiling a possible relation between the mass of the line and its related equivalent forces. In practical way, the ratio between the sum of equivalent loads, expressed in kg, and the corresponding Cold-End mass has been computed for lines featuring different number of brackets and including disparate elements placed in various positions. Some meaningful examples are shown in Figure 4.7.



(a)

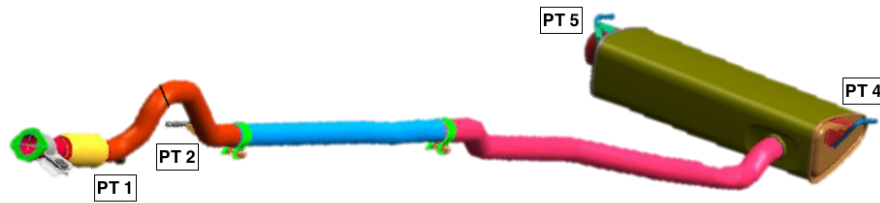


	Equiv. Load [kg]
PT 1	4.83
PT 2	10.03
PT 5	5.98
PT 6	7.00
Tot.	27.84

	Line Mass [kg]
Front	3.17
Cent.	4.46
Rear	3.11
Tot.	10.74

	Equiv. Mass
Tot.	2.590

(b)

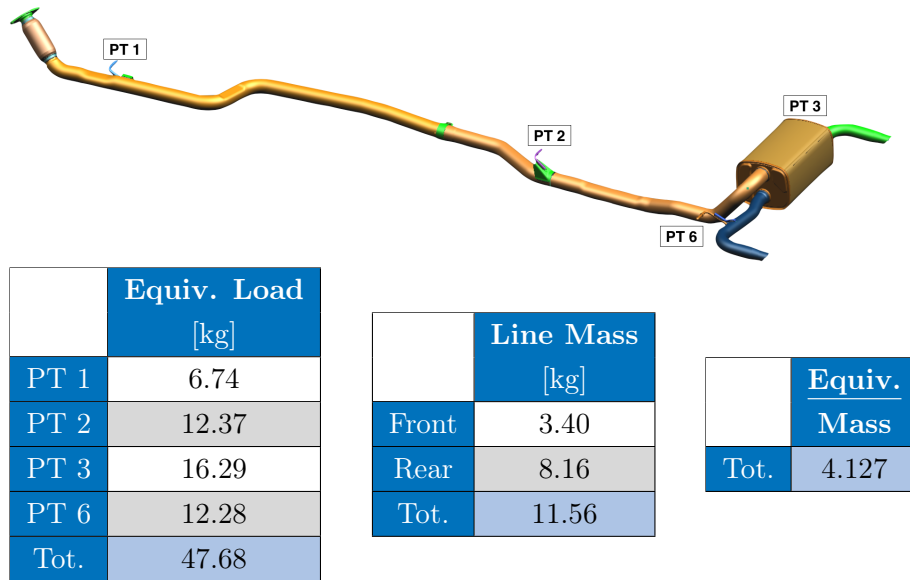


	Equiv. Load [kg]
PT 1	2.75
PT 2	14.27
PT 4	15.24
PT 5	13.10
Tot.	45.36

	Line Mass [kg]
Front	3.00
Cent.	1.44
Rear	8.50
Tot.	12.94

	Equiv. Mass
Tot.	3.505

(c)



(d)

Figure 4.7: Ratios between the sum of the brackets equivalent loads, expressed in kilograms, and the Cold-End mass for models featuring different layouts

As one can immediately infer from the tables of the previous Figure, the presence of mufflers, especially if mounted at the end of the line, acting as a suspended mass, magnifies the damage on the related brackets, thus their corresponding equivalent load. As a result, it has been evidenced that it is not straightforward to deduce the equivalent forces merely from topological and physical characteristics of the line, reaffirming the importance of the RLDA.

Moreover, the lack of correlation among the results presented suggests that the incongruity between the methods shall reside in their inputs. The investigation presented in the next Chapter will be centred on this aspect.

Chapter 5

Vibrational analysis

The results shown in the previous Chapter (Table 4.4) evidence the lack of correlation in the comparison of a static simulation with a dynamic test: from this fact originates the impossibility of reducing the driving test to a single equivalent force.

A further strategy attempted to link up the two methods consists in a frequency analysis of the exhaust system, both in a virtual environment and on physical components. This approach addresses the discrepancies existing in the types of input of the validating methods, which have been stated in the first row of Table 4.1.

5.1 Initial observations

It has been evidenced that the $4g$ static simulation generates forces on the brackets in relation to the centre of gravity and to the mass distribution of the exhaust line. If brackets reaction forces had distributed in the same manner also during the driving test, a relation between the outcomes of the two procedures would have existed. Nevertheless, the examination made on several exhaust lines, in terms of ratios between sum of equivalent forces and total mass of the Cold-End, exhibits a substantial variability of this parameter with the line layout. As a consequence, it has been hypothesised that the line mounted under the vehicle deforms in a different manner, presumably according to its modal shapes. The resulting force distribution would be function of the relative displacement between exhaust hanger bracket and body counter-bracket caused by the natural oscillation of the line, more than by its weight repartition. Obviously this consideration applies when the line is subjected to dynamic input conditions, as it occurs during the test on the Proving Ground.

Objective The purpose of the vibrational investigation is double. The former is to analyse experimental data, namely strains on the brackets and, when

acquired, accelerations, to understand whether the deformations of the line suspended under the vehicle correspond to its modal shapes.

The latter, nonetheless central purpose of the vibrational analysis is to identify some characteristic inputs for the virtual simulation, in terms of an acceleration spectra with respect to the frequency and amplitudes of them, ideally identical for all the vehicles, which could represent of all the different pavements encountered during the driving test and, therefore which could flank the conventional validation procedure. In this manner, the Safety Factors obtained from the virtual computation are supposed to be more correlated with those extracted from the driving test.

5.2 Procedure

The analysis commences from the experimental acquisition of the input accelerations that excite the brackets during the driving test. To accomplish this goal, the vehicle under investigation is equipped with some mono-axial accelerometers, placed in correspondence of the counter-brackets roots. Moreover, other accelerometers of the tri-axial type can be attached to some hanger brackets to better track the behaviour of the exhaust line during the trial. These configurations are shown in Figure 5.1.

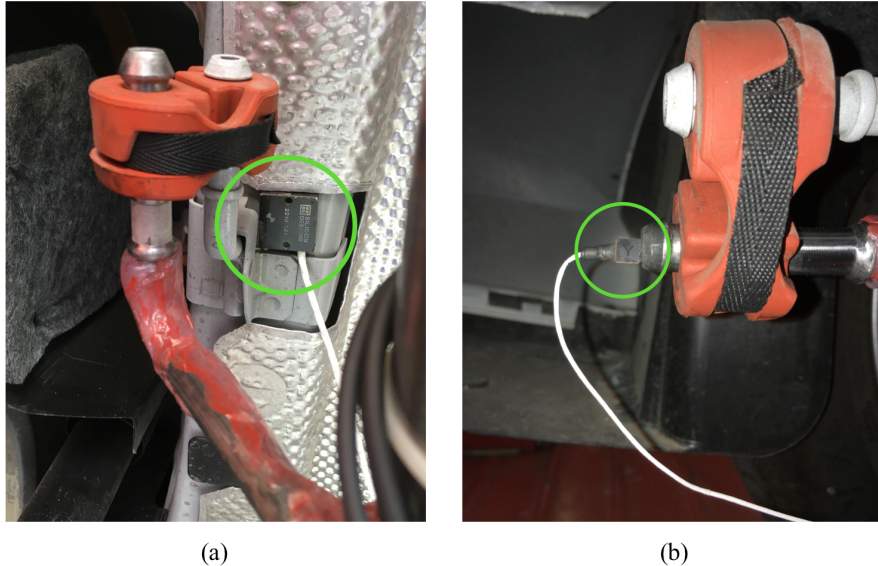


Figure 5.1: *Mono-axial (a) and tri-axial (b) accelerometers applied respectively at the counter-bracket root and at the bracket tip*

These transducers, similarly to what occurs with strain gauges, are connected to an acquisition device which records the time history of the accelerations detected at their application point at a very high rate. Also in this case, an exact replica of the acceleration profile in a virtual simulation would require an unacceptable time, thus it is not practised. To provide a more serviceable

input, after an observation of the gathered data to clean them from misrepresentations, acceleration time histories of each track are stitched together to form an unique sequence, considering that a change in the order of the single samples should not affect the final result. Then, data are filtered in the frequency range which causes the highest oscillations and damage (typically from 5 to 30 Hz) and transposed into the frequency domain exploiting the Fast Fourier Transform (FFT). Accelerations related to frequencies close to zero are discarded because they are principally caused by a variation in ground slope, thus insignificant for damage evaluation, or by software issues when applying the domain transformation. This countermeasure is also taken in case the acquisition is provided as input to the Road Simulation Bench, explained in Section 5.2.1 and Appendix B: to simulate such low-frequencies accelerations, the bench would need to extend its actuators beyond their maximum stroke, hence impairing the effectiveness of the test.

For every pavement, the peak acceleration at each frequency is recorded employing the peak-hold method. These data are then put in matrix form, an extract of which is reported in Table 5.1, having as coordinates the tracks and the analysed frequencies.

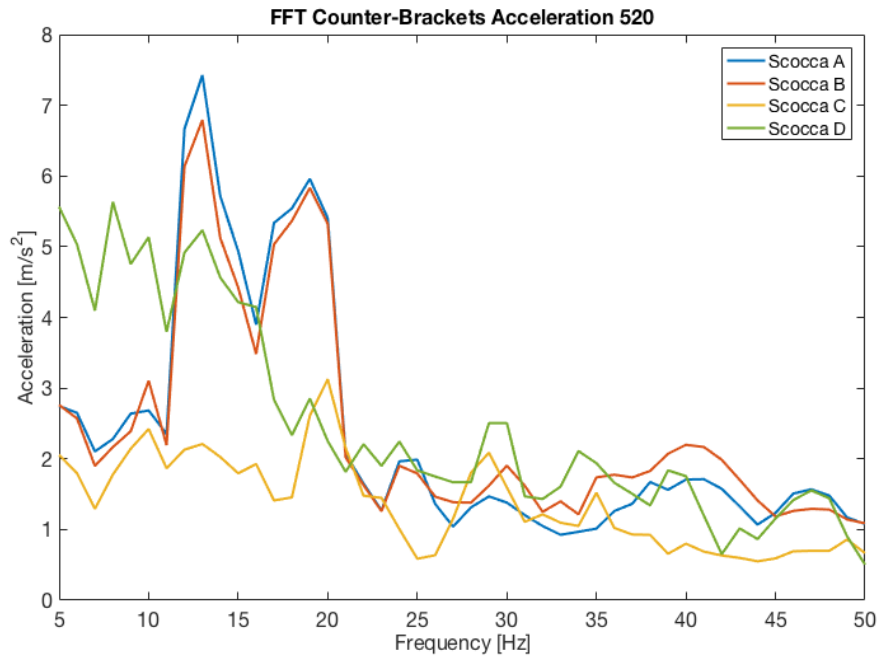
Freq. [Hz]	Accelerations for each type of pavement [m/s ²]					
	Track 1	Track 2	Track 3	Track 4	...	Max.
10	1.42	0.91	3.11	1.63	...	3.11
11	2.10	1.04	2.19	1.78	...	2.19
12	6.14	1.23	3.11	2.80	...	6.14
13	6.79	1.82	4.07	3.73	...	6.79
14	5.12	2.06	3.70	3.10	...	5.12
15	4.42	1.88	3.28	4.17	...	4.42
⋮	⋮	⋮	⋮	⋮	⋮	⋮
50	0.54	0.16	0.10	0.51	...	1.09

Table 5.1: *Extract of the acceleration spectra matrix for each pavement: the overall maximum value of each row, highlighted in red, is tracked to identify the acceleration envelop*

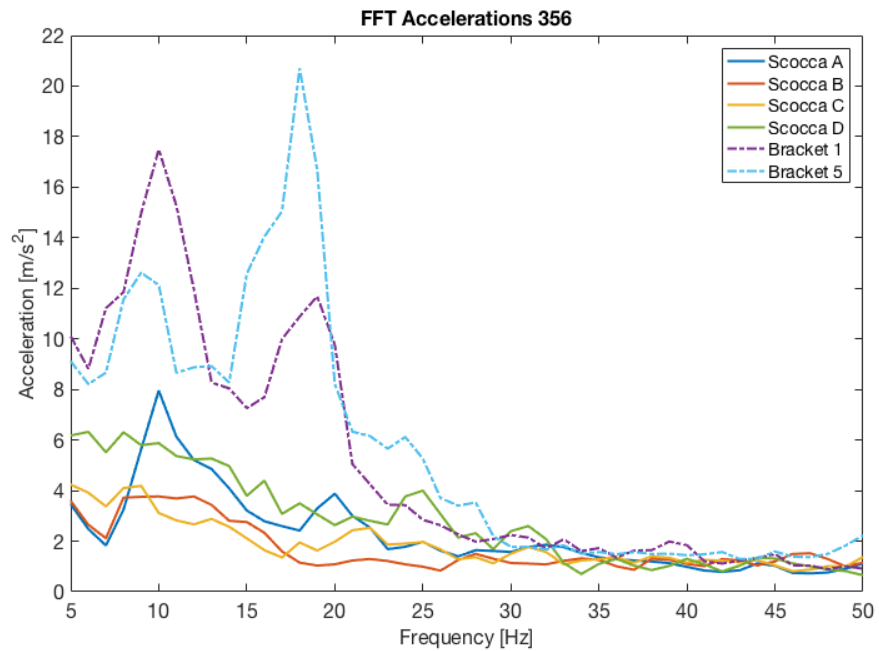
The overall maxima (last column of the matrix) of each frequency batch are then extracted and provided as input for the virtual simulation: their graphical representation is reported in Figure 5.2 for the same models analysed in Section 4.5.1.

From Figure 5.2 (b), comparing the acceleration spectra of the brackets with respect to their relative counter-brackets, one can infer that not all the brackets acceleration peaks are caused by a corresponding maximum of the input, as it occurs around the frequency of 18.5 Hz. This fact already suggests that the line under the vehicle does not merely replicate the displacements of the body, but probably deforms in accordance with its modal shapes. The anal-

ysis in this perspective has been carried after the RSB and virtual vibrational simulations and will be proposed in Section 5.3.2.



(a)



(b)

Figure 5.2: Acceleration spectra relative to two models analysed. Figure (b) contains also the accelerations of the first and last exhaust brackets. To understand the Input/Output relation, their values should be compared to counter-brackets (Scocca) A and D respectively

5.2.1 Calibration at the Road Simulation Bench

Before going in depth with the examination of the road profile, whose excitation spectrum is wide and complicated by the non-null phase between accelerations on different brackets, a preliminary trial has been run to understand how the exhaust system moves under the vehicle, to assess, also for this type of analysis, the gap that exists between virtual simulation and experimental test. For this purpose, it would be necessary to apply a simpler input to the physical exhaust line, namely an oscillation characterized by constant amplitude and frequency, easily reproducible at the computer for the comparison of the results. Since the application of time-invariant inputs is not immediate with the line mounted under the vehicle, the investigation has been carried exploiting the Road Simulation Bench (RSB), available in the Department (Figure 5.3).

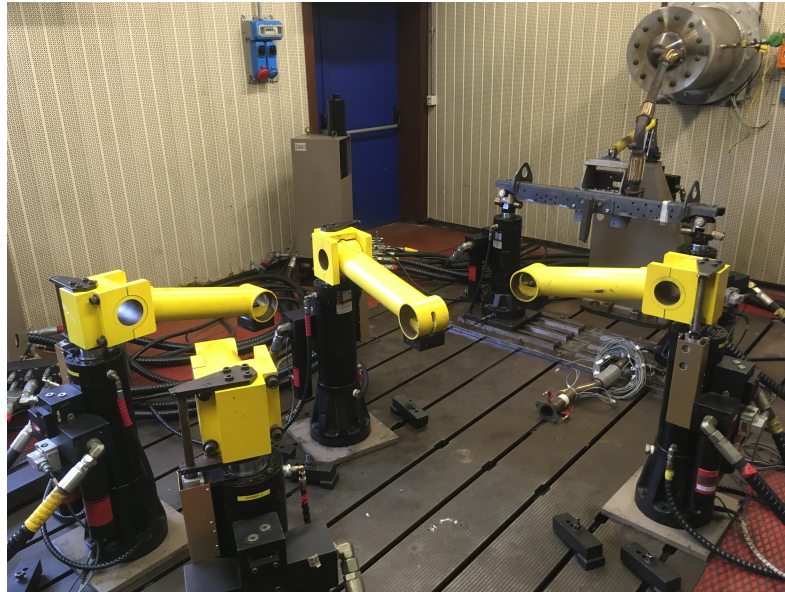


Figure 5.3: *Road Simulation Bench room: the yellow arms are connected to hydraulic actuators reproducing vehicle body accelerations, while the three interlinked jacks, placed on the right of the picture below the gas burner simulate the vibrational behaviour of the engine*

This facility allowed to apply as inputs pure tone sinusoidal displacements or sweeps in frequency at fixed amplitude, in phase among each other, to the counter-brackets of an instrumented exhaust line to compare the outcomes of a physical specimen to those of a virtual analysis. Deeper notions about the purpose and the details of the Road Simulation Bench are reported in Appendix B.

Bench set up To run the acquisition activity, which has been carried for one of the models previously analysed, the line is fixed to the hydraulic jacks of the bench, which reproduce vehicle counter-brackets, in the same manner

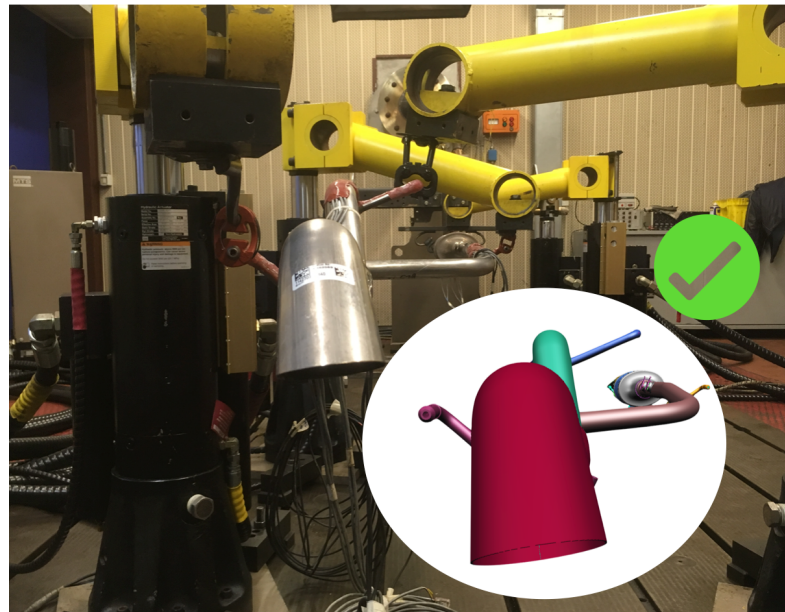
and using the same elastic isolators prescribed for the normal operation under the car. To set up the test properly, each hydraulic actuator must be disposed close to the exhaust system, placed initially on the ground, in correspondence of the brackets avoiding any possible interference between the specimen and the actuator arms that could arise during operation. Then, the reproduced counter-brackets are fastened to the tips of the actuator arms, as highlighted in Figure 5.4. That location corresponds also to the zone in which mono-axial accelerometers, required by the bench as feedback signal, are attached.



Figure 5.4: *The same disposition and shape of vehicle counter-brackets is cloned for the bench simulation. These features are rigidly connected to actuator arm tips through bolts*

Once completed this operation, the oil pump is switched on, at reduced power, to provide enough pressure to maintain the actuators in their neutral working position, namely at mid span of the overall displacement. At this point, with the half-raised actuators, it is possible to start suspending the line with the proper isolators. This carefulness is taken to have a homogeneous reference relative to which the line is disposed and to avoid differences in height, caused by residual pressures in the cylinder, at rest that would introduce undesired distortions during system operation.

Once the line is suspended, it is important to verify that its position corresponds to the designed one, that isolators are not twisted nor stretched in an unnatural manner and that the vertical movement of the hydraulic jacks does not produce displacements of the line others than vertical. The comparisons between the actual mounting conditions and the designed ones are depicted in Figure 5.5. Only after these checks have been terminated, it is possible to definitively fix the actuator bases to the ground seismic mass.



(a)



(b)

Figure 5.5: *Rear (a) and global (b) view of the exhaust line mounted on the bench and comparison with its design condition*

Test After the connection of the acquisition devices for strains and accelerations, the test can be launched. This kind of trial performed at the RSB is largely simpler than the reproduction of a durability test explained in Appendix B and does not require any calibration of the bench itself.

For each actuator the displacement law is defined by the following parameters:

- type of signal, such as sinusoidal wave, triangular wave, ect.;
- amplitude, namely maximum displacement from the rest condition of the actuator;
- frequency of the signal;
- phase angle with respect to any other actuator;

- time duration of the trial.

In the presented case, the most significant tests have been carried choosing as inputs a constant-frequency, fixed-amplitude sinusoidal displacement of each actuator with null phase among each other and some frequency sweeps, from 0 to 50 Hz, always with the actuators in phase, keeping constant the amplitude: this last case generates on the counter-brackets an acceleration increasing with a quadratic law.

Before launching the test, a synchronization signal is fed simultaneously to both acquisition devices to allow, during data post-processing operations, a correct superposition of causes (accelerations of the counter-brackets) and effects (brackets strains), helpful to understand any possible relation among them.

The outcomes of this trial will be compared with those coming from the virtual simulation of the exhaust line to which similar inputs are applied.

5.2.2 Virtual Vibrational analysis

The computational vibrational simulation exploits the same configurations already settled for the static $4g$ simulation. Despite this, since the test presents different boundary conditions and desired outputs, some adaptations must be applied.

The first operation to be carried is to modify the stiffness of rubber isolators and of the flexible decoupler. While this characteristic is a constant value in static conditions, when the elastic element is subjected to dynamic deformations, its response varies as function of the excitation frequency. In Figure 5.6 this characteristic is shown for two generic rubber isolators.

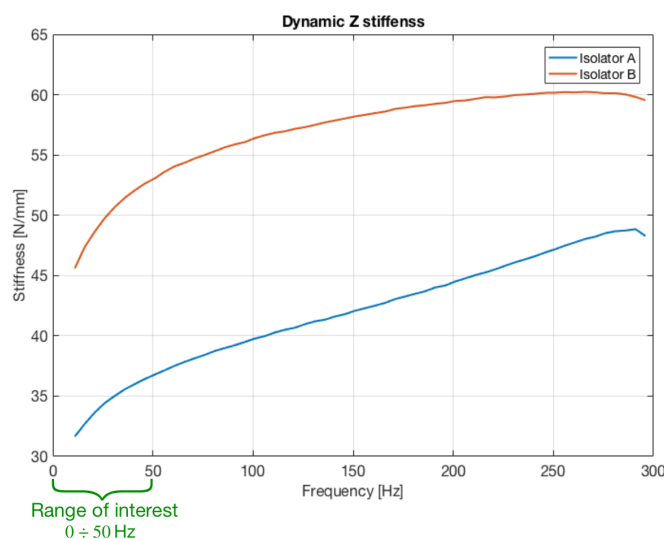


Figure 5.6: Variation of the dynamic stiffness of two rubber isolators as function of the frequency

For very low excitation frequencies it is not possible to deduce the stiffness from the previous chart: for this reason, the static stiffness value has been assumed for a frequency $f = 0$ Hz. The other missing data are obtained by interpolation.

A similar behaviour can be recognised for the damping coefficient of elastic elements (Figure 5.7).

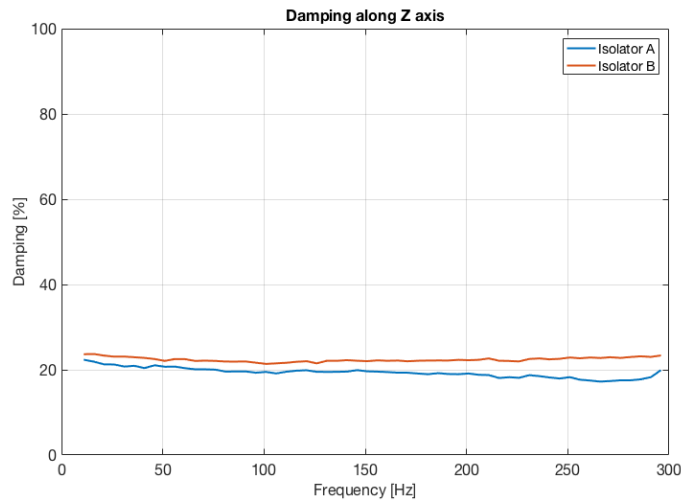


Figure 5.7: Variation of the damping coefficient of two rubber isolators as function of the frequency

These properties are attributed to the elastic *CBUSH* elements using the *PBUSH* card. It is necessary to specify there the pointer to a table containing the dynamic characteristics of the related element: thanks to this expedient, the software automatically selects the proper stiffness and damping depending on the instantaneous frequency that solicits the element.

In a similar manner, also material hysteresis has to be taken into consideration: this is done applying a 2% damping factor to all metallic elements over the whole frequency range.

Afterwards, it is necessary to declare the Dynamic Loads, defining *DLOAD* properties. Similarly to what occurred for the stiffness, each load too is defined in a table, expressing its variation law in the frequency domain. For the purpose of the present investigation, these tables contain the counter-brackets acceleration spectra measured during the driving test (reported graphically in Figure 5.2) and during the RSB trial. In contrast to the static analysis, in which the whole structure was subjected to a distributed load, these dynamic actions must be applied in correspondence of the counter-brackets constraints only, as represented in Figure 5.8: to achieve this, the *DLOAD* container must include the identification numbers of the application nodes and the direction along which the load must be applied.

Eventually, before launching the simulation, it is customary to define spe-

cific sets of node IDs for which the output is required: this strategy permits to shorten the computational time, which, with these expedients, is approximately 15 minutes.

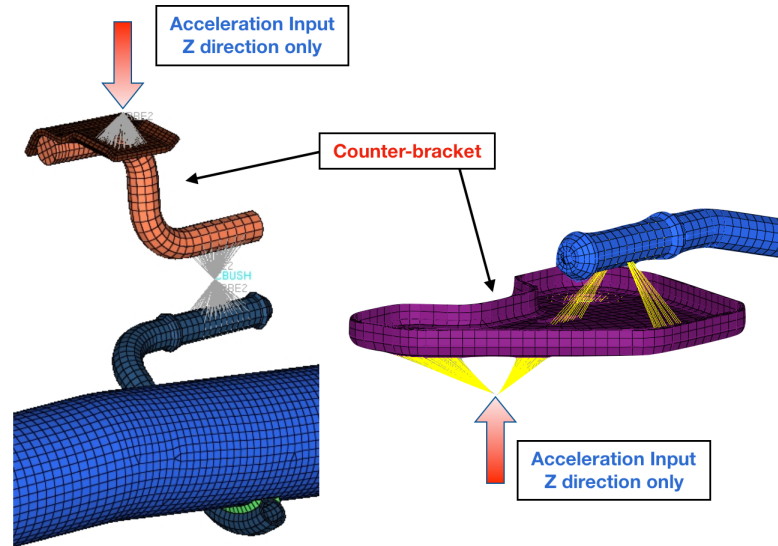


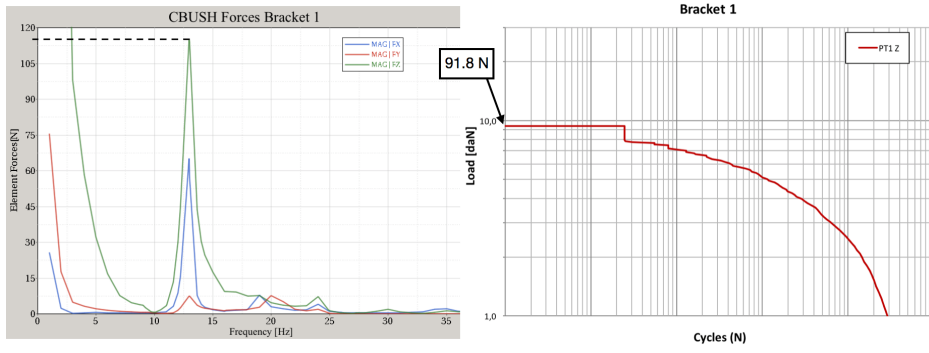
Figure 5.8: Application points of the input accelerations for numerical vibrational analysis

5.3 Results comparison

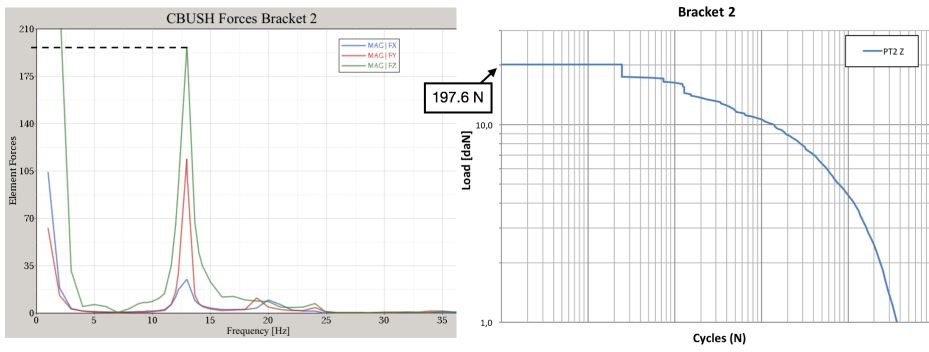
5.3.1 Simulation of road acceleration spectra

The first trials were aimed at simulating the effect of the counter-brackets accelerations spectra measured on the Proving Grounds (Figure 5.2). The outputs of the numerical analysis selected for comparison with the experimental test are the spectra of the reactions at the isolator elements. These forces are presumed to equal brackets loads, calculated according to the experimental procedure, (strain value times the calibration coefficient) for given testing conditions. Going deeper in the details, since the input of the simulation is constituted by the peaks accelerations encountered during the road test, it is straightforward to imagine that the maximum bracket force is caused by the maximum acceleration. In particular, the global maximum of each bracket is supposed to correspond to the highest load registered in the Rainflow diagram.

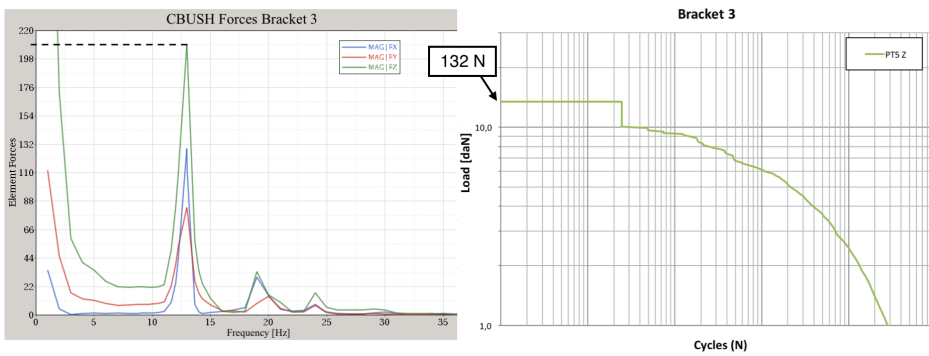
As a matter of fact, this consideration did not prove to be valid generally, since the correlation has been found only for few brackets. Figure 5.9 and Table 5.2 show the absence of correlation between the outcomes of the two methods. The discrepancies can be ascribed to the simplifications introduced in the model and to the loss of information, in particular of the relative phase among the counter-brackets accelerations, which occurs when transposing data from the time domain to that of the frequency.



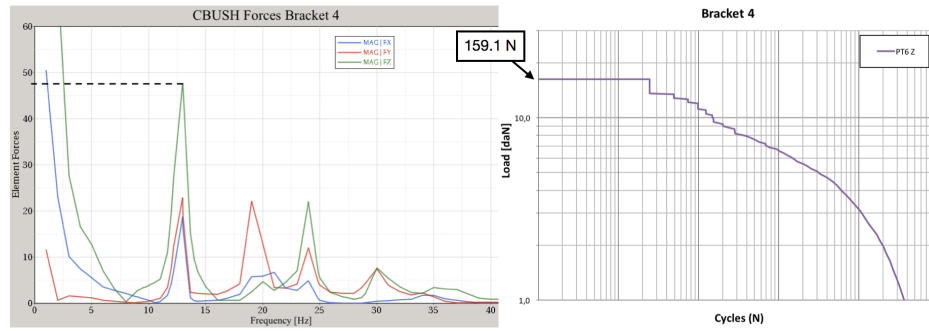
(a)



(b)



(c)



(d)

Figure 5.9: Graphical comparison between brackets (experimental) and CBUSH isolators (virtual) maximum forces obtained applying as input of the simulation the road acceleration spectra. Notice: the portion of the spectrum at very low frequencies has to be neglected

	Freq. [Hz]	Numerical CBUSH [N]	Proving Ground Max [N]	$\Delta\%$ [-]
(a) PT 1	13	116	91.8	-20.8%
(b) PT 2	13	196	197.6	1%
(c) PT 5	13	208	132	-36.5%
(d) PT 6	13	48	159.1	231%

Table 5.2: Comparison between isolators CBUSH (virtual) and brackets (experimental) maximum forces: the inputs for the simulation are the acceleration spectra obtained from the driving test

5.3.2 Modal deformation

RSB test Comparing the inputs, reported in Figure 5.2 (a), with the outputs of the numerical analysis of Figure 5.9, it can be evidenced that the line deformations concentrate around the excitation frequency of 13 Hz, while the local acceleration peak around 18 Hz is filtered out.

An analogous behaviour has been observed on another line (the one of the 356) which has been mounted on the Road Simulation Bench: in spite of an excitation over the whole frequency range from 0 to 50 Hz, the brackets response, in terms of accelerations, condensate around few frequencies. This Input/Output relation is illustrated in Figure 5.10.

The quadratically increasing trend of the counter-brackets accelerations is caused by a linear growth of the frequency at a fixed amplitude of the displacement. The descending part, on the other hand, is attributable to the impossibility of the system of satisfying both requests of frequency and amplitude: the control strategy prioritizes the tracking of the former, releasing the constraint of the latter.

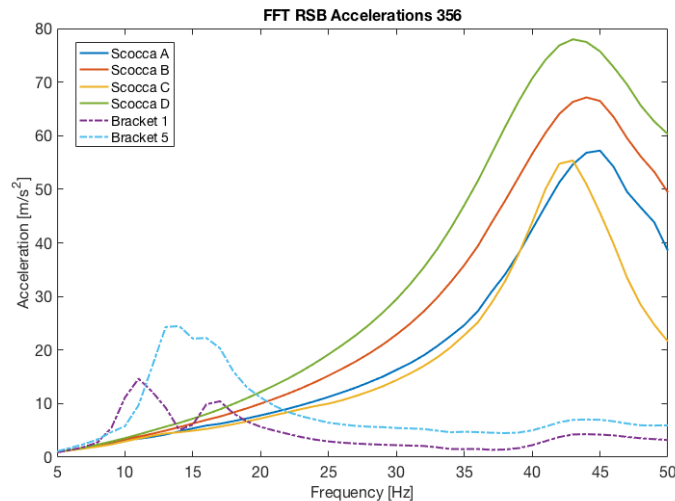


Figure 5.10: Acceleration spectra of the model tested at the RSB. The inputs (Scocca) are the accelerations imposed by hydraulic actuators, while dash-dotted line tracks the accelerations at the tips of brackets 1 and 5

Looking at the modal analysis outcomes, these frequencies reveal to coincide with resonances of the whole Cold-End. From this intuition, the idea of analysing the road acquisitions in terms of modal deformations has been advanced.

RLDA time-frequency analysis In this perspective, several strains and accelerations acquisitions of the driving tests have been examined in the frequency and time domain contemporary by realizing some colour maps. These graphs collect in an unique chart several acceleration or strain spectra calculated at each time interval, as illustrated in Figure 5.11.

The colour maps are obtained shortening the time period between two FFTs computation, to have smoother transitions, and expressing the vertical (amplitude) development with a chromatic scale.

The advantage brought by such a representation is the possibility to analyse the frequency spectrum in time to understand the input/output behaviour of the exhaust line. In particular, the availability of colour maps representing counter-brackets accelerations and brackets strains allows to identify resonances, which are supposed to occur whether the line response concentrates around particular frequencies, even if the input has marginal amplitude related to said frequency. Among all the proving grounds, the diagrams proposed and analysed in the following are referred to the most severe ones.

The first batch of colour maps is related to a track paved with cobblestones. The initial 200 m, featuring a totally random surface profile, are covered at a speed within 25 to 30 km/h, which is reduced to 20 to 25 km/h for the

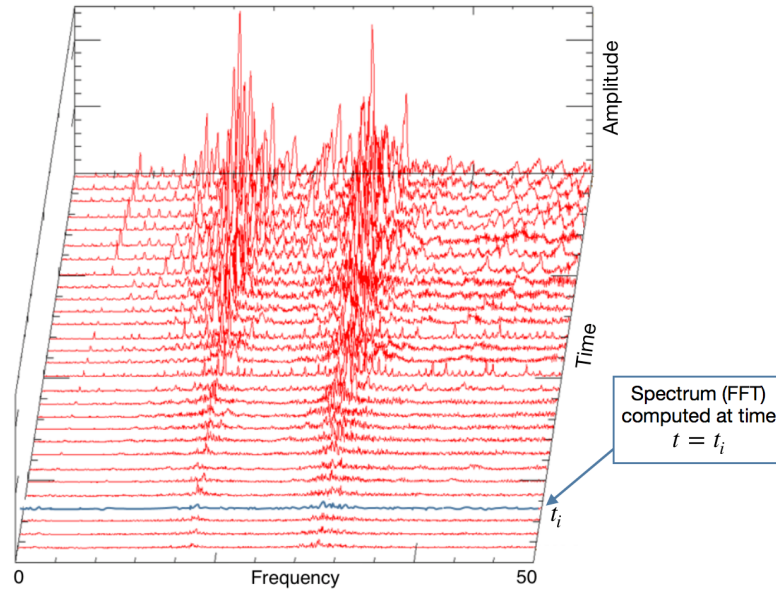


Figure 5.11: *Scheme of the data contained in a colour map*

subsequent 200 m. In this last portion, the cobbles are disposed to produce an oblique undulation with respect to the lane axis, as reported in Figure 5.12.

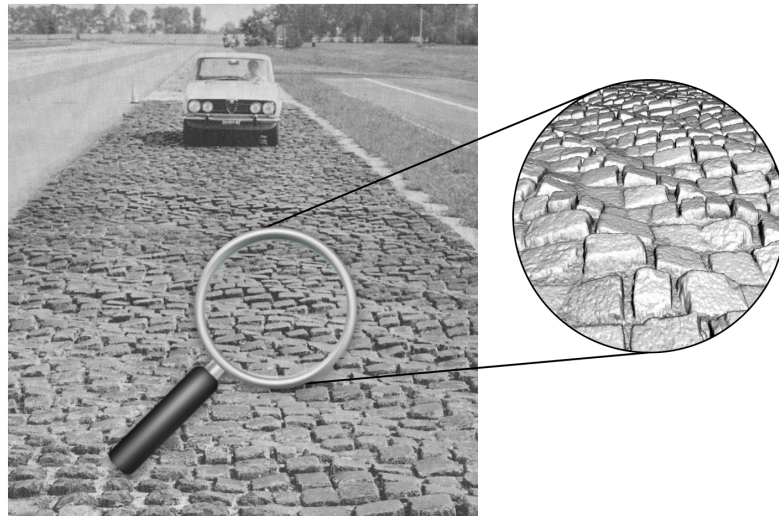
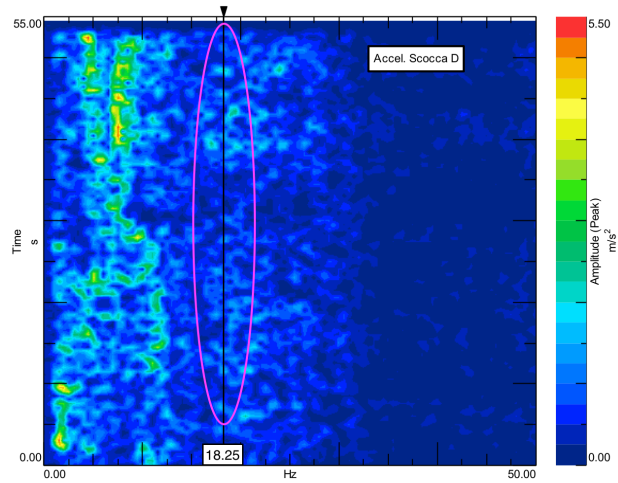


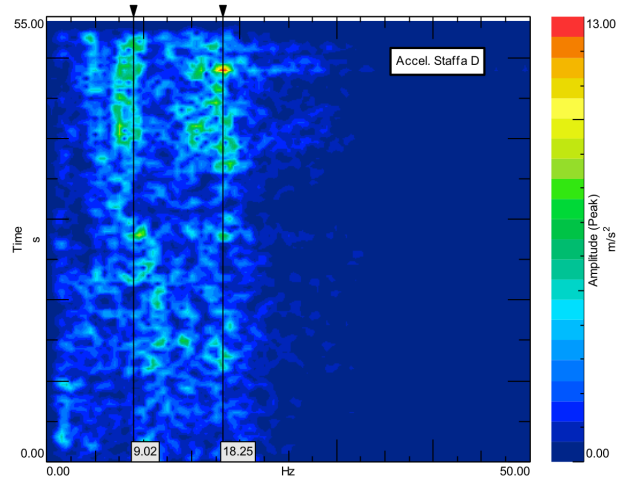
Figure 5.12: *Surface profile of one of the most severe Proving Grounds. Colour maps are referred to acquisition on this track*

Despite the last regularity highlighted in the pavement, this track is known to produce a random excitation on the exhaust line over the whole frequency spectrum from 0 to 30 Hz.

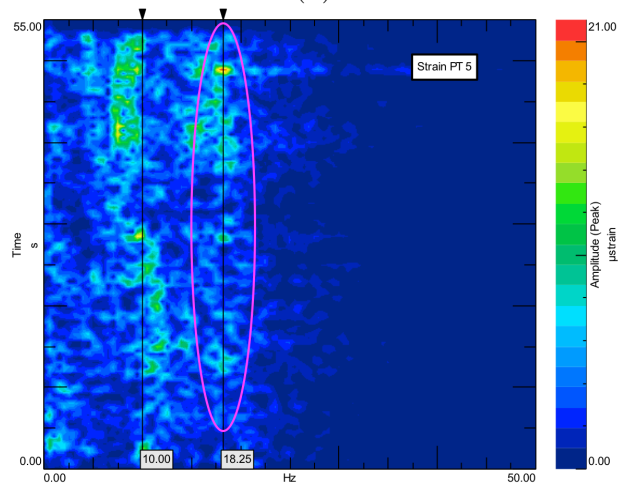
The three plots reported in Figure 5.13, referred to the tailpipe hanger bracket, represent the spectra over the time of the counter-bracket acceleration (a), the input, those of the bracket acceleration (b) and of the bracket strain (c), the outputs. The randomness of the road profile is evidenced by the absence of strong peaks of counter-brackets acceleration within the fre-



(a)



(b)



(c)

Figure 5.13: Colour maps of tailpipe counter-bracket (a) and bracket (b) accelerations and corresponding bracket strain (c) of 356 model exhaust to highlight the Input/Output relation. The line resonance is evidenced in purple

quency range (at least, up to 30 Hz). The line resonance can be perceived looking across the three plots at fixed frequencies. Focusing on the frequency of 18.25 Hz, it is noticeable that non-negligible or even the maximum bracket strains (c) and accelerations (b) concentrate around this frequency, although the corresponding input acceleration (a) is moderate, as highlighted in the Figure. The hypothesis of line resonance is confirmed by the modal shape assumed at 18.5 Hz, shown in Figure 5.14.

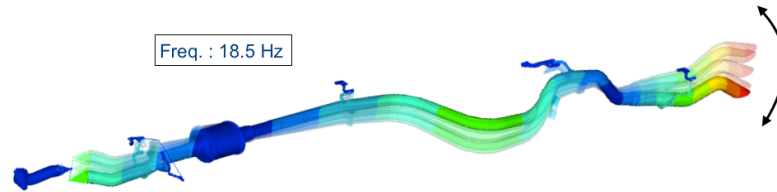
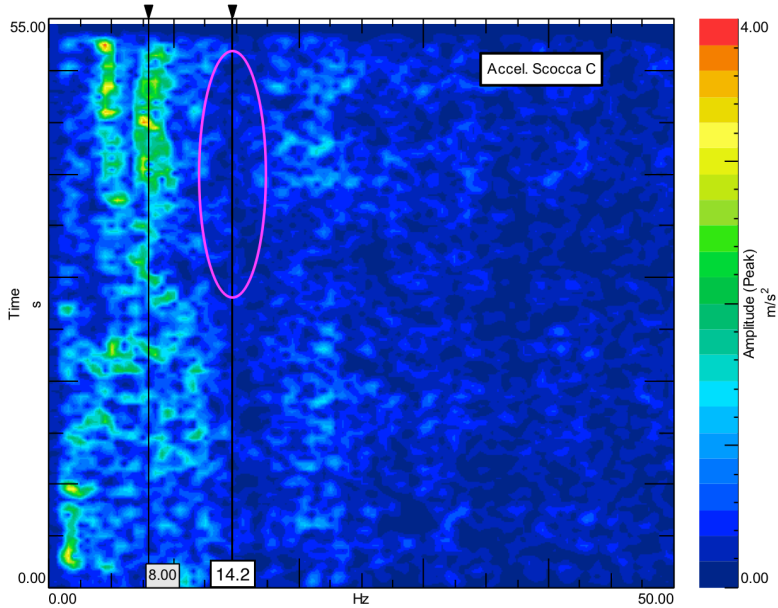


Figure 5.14: *Modal shape of the 356 model line at 18.5 Hz: the highest deflection is localized at the tailpipe*

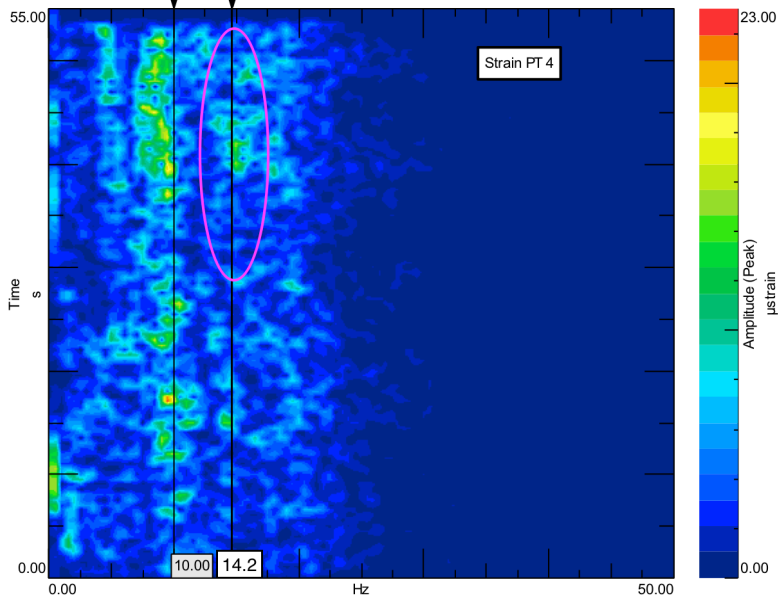
A comparable behaviour, caused by the resonance around 13 Hz, occurs for the fourth bracket of the same line. Similarly to the previous one, Figure 5.15 contains counter-bracket acceleration (a) and the related bracket strain (b). It can be observed that a relevant deformation is present against a lack in the input, in the neighbourhood of 14.2 Hz. Also in this case, the conjecture of the resonance is in accordance with the natural deformation at 13.1 Hz reported in Figure 5.16.

Figure 5.17, representing the same data referred to the penultimate bracket the 520 exhaust system, reinforces what has been supposed in the previous paragraphs. 10 Hz is in fact the natural frequency of this line, causing the deformation reported in Figure 5.18.

The amplification of a weak input is flanked also by the attenuation of intense accelerations. Figure 5.19, showing again the same data, points out that the strong accelerations measured at low frequencies are completely filtered out and do not cause bracket deformation.



(a)



(b)

Figure 5.15: Colour maps of the fourth counter-bracket acceleration (a) and bracket strain (b) of the 356 line

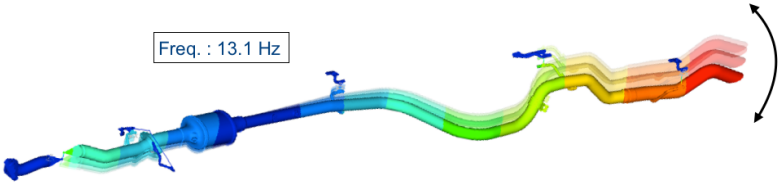
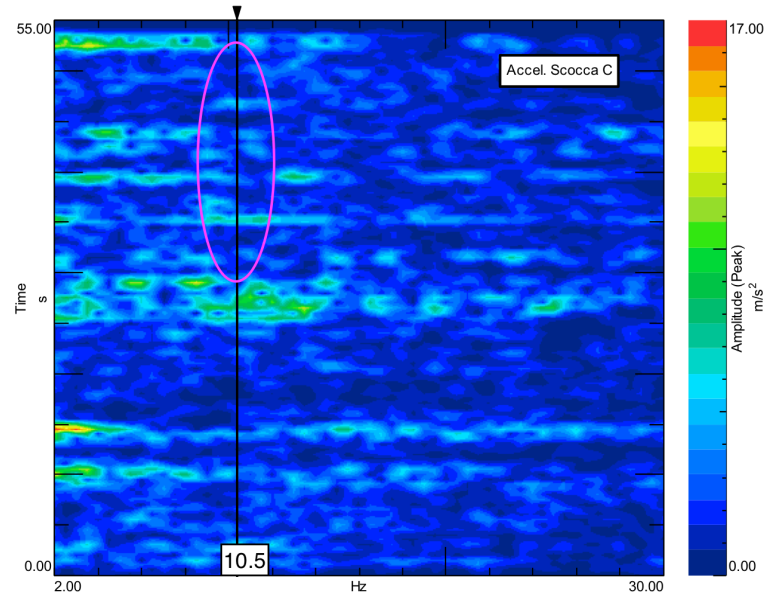
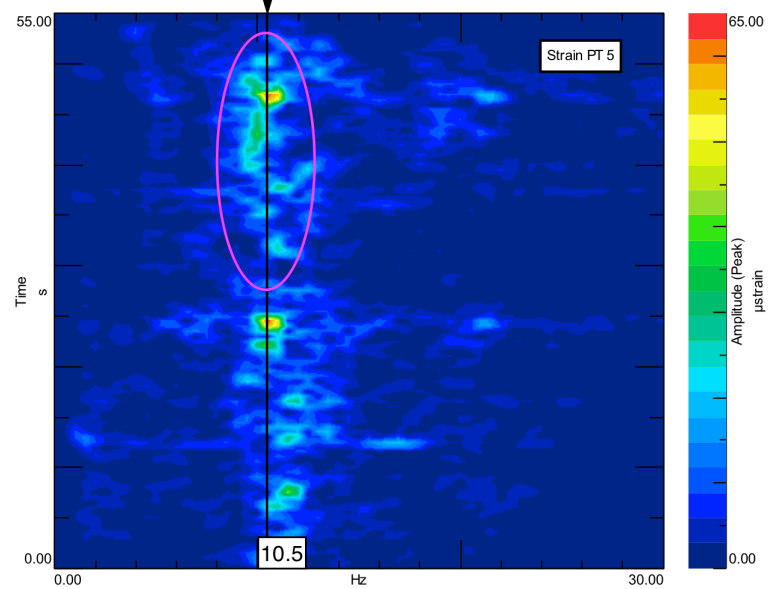


Figure 5.16: Modal shape of the 356 line at 13.1 Hz



(a)



(b)

Figure 5.17: Colour maps of fourth counter-bracket acceleration (a) and corresponding bracket strain (b) of 520 model exhaust line

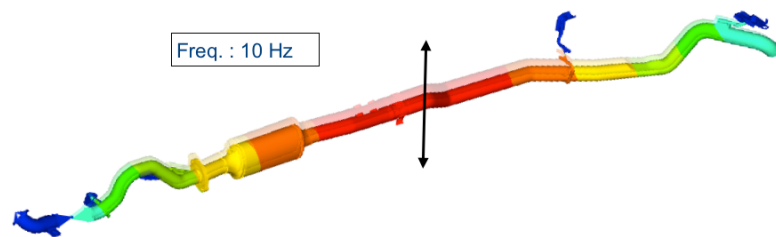


Figure 5.18: Modal shape of the 520 line at 10.1 Hz

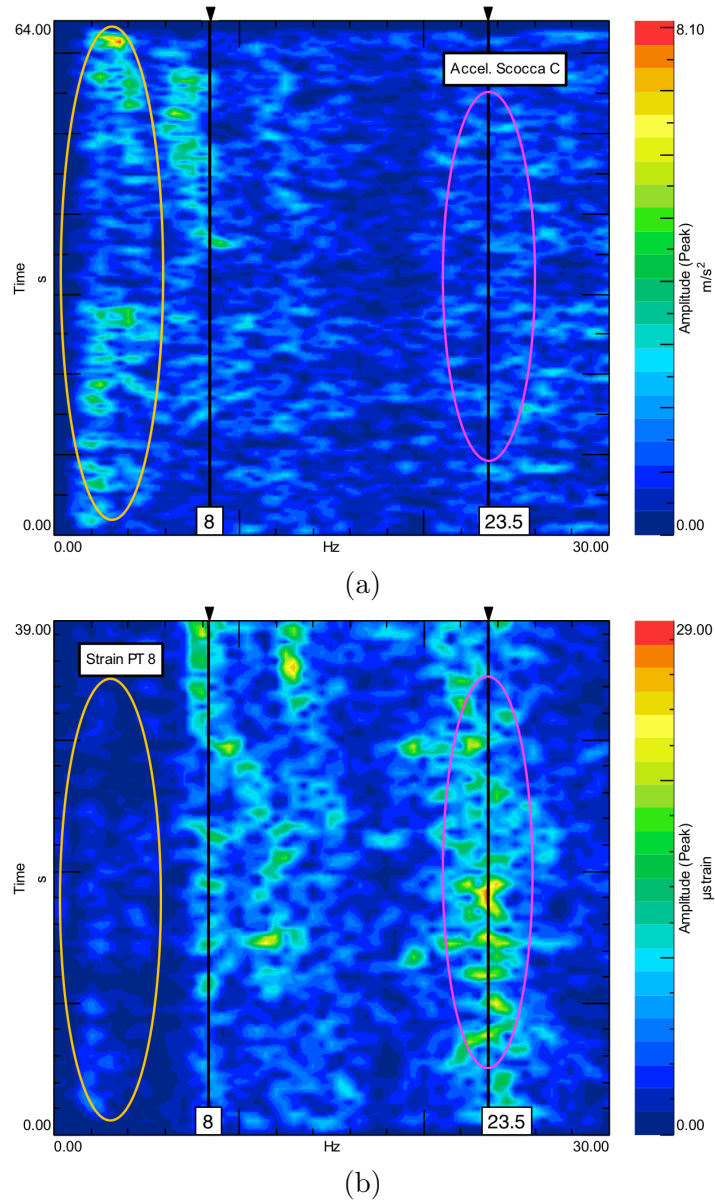


Figure 5.19: Colour maps of tailpipe counter-bracket acceleration (a) and corresponding bracket strain (b) of 263 model exhaust line. The input attenuation at low frequencies is evidenced in yellow

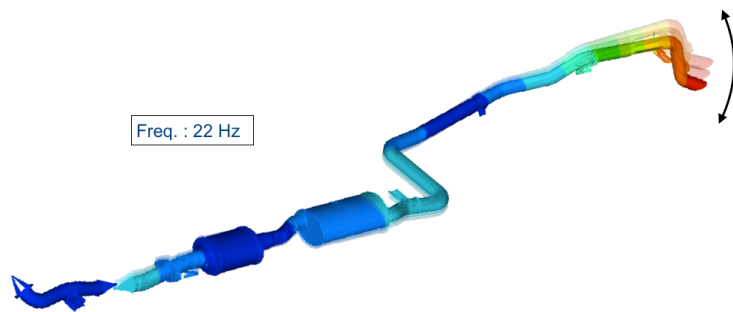


Figure 5.20: Modal shape of the 263 line at 22.8 Hz

5.4 Comments and observations

The results shown confirm the hypothesis according to which the exhaust line assumes its modal characteristic shapes when subjected to oscillating inputs. Nevertheless, a certain difference between resonance frequencies obtained from numerical modal analysis and those revealed by the colour maps can be noticed. This discrepancy can be mainly attributed to the constraints, absent in the virtual analysis, to the assumptions made for the isolators characteristics and to the damping coefficient of 2% assigned to the material for the calculation. As explained this a *de facto* value selected for vibrational analyses: correlation tests should be carried to assess a more appropriate damping coefficient.

The subsequent step would be the application of such an analysis for the validation. To achieve this, in the first instance, it is necessary to determine the acceleration amplitudes and the frequency range, namely the spectrum, to be applied as input of the numerical analysis to reproduce the experimental road test in a virtual environment. From the colour maps reported in this Chapter and from the charts of Figure 5.2, the frequency range of 0 ÷ 30 Hz appears to be suitable for the purpose. For what concerns the acceleration amplitude, things are slightly more complex. The experimental input depends on the specific vehicle characteristics (mass, suspension behaviour, wheelbase, etc.) and, thus it is unlikely to identify a general input applicable to all the cars. For this reason, the first trials have been performed with the most simple solution, generally valid, such as a fixed amplitude. Then, the outputs of the calculation have been compared to the measured values: the simulated maxima have been multiplied by tailored coefficients to minimize the difference with respect to the highest load of the cumulative, making the results comparable. Owing to the fact that an increase in the input amplitude would cause a proportional growth of the corresponding output, multiplying the initial input by the aforementioned coefficient one is supposed to obtain the desired amplitude. The outcomes of the process just described are collected in Table 5.3, in which $\Delta\%$ has been obtained with the previously mentioned Equation 4.5.

	Max Exp. Stress [MPa]	Max Vibr. Stress [MPa]	Freq. Vibr. [Hz]	Max Exp. Force [daN]	Max Vibr. Force [daN]	Max Loads $\Delta\%$
PT A	39.6	36.3	15	7.94	6.96	14%
PT B	50	41.4	15	9.06	9.48	-4%
PT C	50	66.6	15	9.03	10.86	-17%
PT D	89.7	82.8	26	11.43	11.64	-2%

Table 5.3: Comparison of the outcomes of experimental road test and vibrational simulation. The reduction of the absolute value of the percent difference between the methods highlights a better correlation

As it is immediate to infer from the last column that the distance among the outcomes of the two analysis methods has decreased in absolute value with respect to the results proposed in Table 4.4. This fact indicates that the

After an iteration of this process for several vehicles and exhaust lines, it should be possible to extract the values for the validation through statistical computations.

Last but not least, an element that needs a dedicated tuning is the Safety Factor. Since the examination conditions are different from the static ones, it is necessary to verify whether the Haigh diagram is still a satisfactory basis for comparison or to identify the parameters to be checked with their corresponding thresholds. Another alternative could be to extract a damage level corresponding to the vibrational analysis, to be related to the experimental one. Eventually, to better correlate the virtual evaluation with the testing procedure, load cumulative curves could be generated starting from the peaks stresses highlighted by the numerical analysis, always retrieving the corresponding forces through the calibration coefficients. Actually this procedure would require a general shape of the cumulative, which would be rescaled according to the highest load. An initial approach to this problem is proposed in the next Chapter.

Chapter 6

Global cumulative curve

Along the evaluation of the hanger brackets damage, it has been evidenced that the cumulative load curves feature always a recurring shape, although the values of the forces and number of cycles may vary in relation to the element analysed. As mentioned at the end of the last Chapter, to evaluate the numerical damage on exhaust brackets starting from the load that causes the maximum stress during the vibrational analysis, it would be necessary to know the shape of the Rainflow curve. In the following, an attempt to obtain a global curve is proposed.

6.1 Procedure

In order to obtain a result valid, in principle, for all conventional¹ brackets, the computation has been made on a statistical basis: data of several vehicles and exhaust layouts, gathered by the Company during its testing activities, have been collected and elaborated. In particular, for the computation of the average normalized curve presented in this Thesis, 156 cumulative curves of the same number of exhaust hanger brackets have been employed.

To disregard the differences in terms of maximum loads, the curves have been normalized by dividing each ordinate value by the maximum force measured on the corresponding bracket. In this manner, the ensuing plots, sharing the same ordinate axis, can be superimposed, as shown in Figure 6.1, to assess the effective shape correspondence.

Despite the high variation perceived at the right tail of the plot, mainly concerned with infinite fatigue life, the initial expectations are satisfactorily met, since the lines superposition in the left and central zone of the chart is unobjectionable. These are the areas primarily involved in the damage estimation, thus a lower spread of the data would allow to deduce results with a wider applicability basin.

¹It can happen that particular shapes or specific customer requests do not allow the straightforward application of such a result.

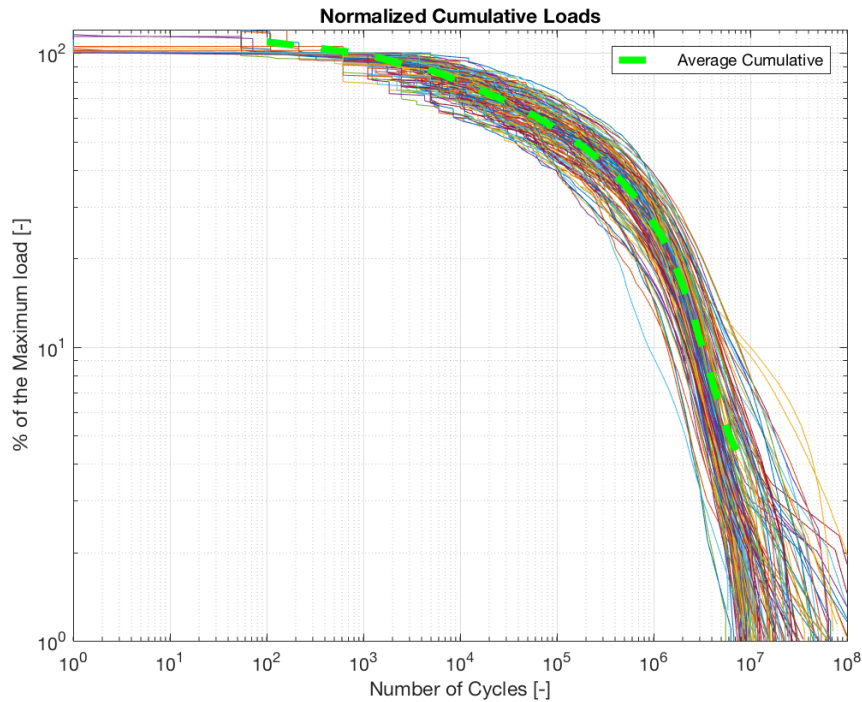


Figure 6.1: *Superposition of several cumulative curves normalized with respect to their maximum loads*

Afterwards, the trend line has been obtained by making the average of all the curves. To avoid an excessive data fitting in the tail zone, which would impair the effectiveness of the global cumulative, the computation of the average curve has been truncated to 10^7 cycles.

6.2 Result

To better visualize the dispersion of data, the standard deviation has been computed and the curves at $\pm 2\sigma$ plotted. The final result is reported in Figure 6.2.

The plausible applications of such a result are, as mentioned, the procurement of a cumulative curve from a numerical simulation, rather than from a driving test, to extract the damage and the safety factor of brackets.

Another elements for which a statistical analysis could be profitable are Wöhler's curves: by averaging the results obtained during the fatigue characterization of numerous brackets, it would be possible to derive an average fatigue curve, along with its probabilistic bands, to be employed for all the brackets.

If the dispersion of such curves would be excessive, it could be interesting to investigate whether a relation between hanger characteristics and the corresponding fatigue curve could be found. In this way, the fatigue test on specimens at the bench could be avoided, since the proper limit curve should

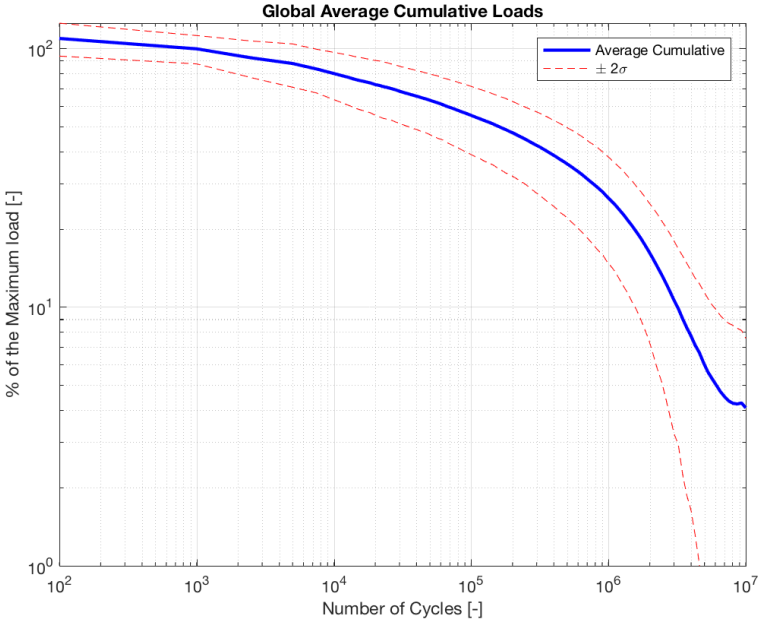


Figure 6.2: *Global normalized cumulative curve with the dispersion band of $\pm 2\sigma$*

be retrieved from the model built.

Chapter 7

Conclusion

Although not all the analyses that have been performed and proposed in this Thesis brought to the result expected at the beginning, each of them has provided its little contribution to achieve a more significant result. Many times the best intuitions come out when the austerity of the traditional methods and convictions falls.

The correlation analysis discussed in this work allowed to demonstrate how the exhaust line deforms under the vehicle during its operation. This finding triggers the possibility of applying a virtual simulation that better reflects the real working conditions of the exhaust line, especially for what concerns the loads distribution.

The value of the investigation is confirmed by the reduction of the distance between experimental and numerical validating procedures obtained with the innovative solutions proposed. Last column of Tables 4.4 and 5.3 evidence how the vibrational analysis approaches the experimental results with respect to the conventional application of the $4g$ static acceleration.

As a matter of facts, the traditional CAE validation method will not be substituted until the proper inputs for the vibrational simulation are found and the process would demonstrate reliable. This is the field in which future developments are supposed to be focused. Whether the continuation of the investigation would allow to attain satisfactory results, the innovative procedure can be phased-in for a future application.

In this preliminary phase, the studies followed a reverse path, starting from the results to obtain the inputs: this regression process is the typical strategy applied to extract a model from a batch of available outcomes and the corresponding sources. Nevertheless, the global objective is to identify a proactive validation method, which would produce the require results in a shorter time, perhaps avoiding some (or any) physical test.

Appendix A

Strain calibration factors

In this Appendix, some of the strain calibration factors, in particular those related to the same models analysed in Section 4.5.1, are reported. Similarly to what has been evidenced for the stress coefficients in Table 4.3, also in this case the differences between the two validating methods are contained. It is worth to remind that the most impacting source of error is the imprecision in the application point of the load during the calibration and in the selection of nodes homologous to the strain-gauged ones. Nevertheless, in similar conditions, the results of both studies are correlated.

520 - No muffler

	Deformation/Load [μ strain/daN]		
	Experim.	Virtual	$\Delta\%$
PT1 E1	11.2	10.5	6 %
PT1 E3	-11.2	-10	12 %
PT2 E1	11.6	10.9	6 %
PT2 E3	-13.0	-11.3	15 %
PT3 E1	13.0	11.7	11 %
PT3 E3	-11.8	-9.6	23 %
PT4 E1	8.6	7.4	17 %
PT4 E3	-8.0	-7.8	3%

Table A.1: *Experimental and numerical strain calibration coefficients for the model 520 without rear muffler*

356

	Deformation/Load [μ strain/daN]		
	Experim.	Virtual	$\Delta\%$
PT1 E1	10.1	6.5	56%
PT1 E3	11.2	8.31	35 %
PT2 E1	9.5	8.3	15 %
PT2 E3	10.4	10.5	-1 %
PT3 E1	11.4	13.9	-18 %
PT3 E3	14.6	13	12 %
PT4 E1	15.8	15.7	1 %
PT4 E3	13.6	14.4	-5 %
PT5 E1	14.9	14.8	0 %
PT5 E3	12.9	13.2	-2 %

(b)

Table A.2: *Experimental and numerical strain calibration coefficients for the model 356*

Appendix B

Road Simulation Bench description

The Road Simulation Bench was built as a solution to simulate the thermo-structural durability test of the complete exhaust system, following the car makers designated Proving Ground, with the aim at defining the reliability level of the components on the field. Conventionally, the car makers perform on-vehicle tests on specific tracks to assess both vehicle and components reliability. The advantages of the RSB are:

- the complete automation of the test, which requires neither the constant presence of an operator nor the availability of the vehicle for the whole trial, but exclusively for the data acquisition;
- the shortening of the time required to run the analysis, from three months of driving tests to three weeks of simulation;
- the increased repeatability of the conditions over time (influence of the driver and driving conditions);
- the possibility of testing several lines of the same vehicle model, since their input are in principle the same;
- etc.

The bench is constituted by seven hydraulically powered actuators, similar to hydraulic jacks, mounted in a vertical direction. Three of them are aimed at reproducing the engine oscillations, thus can reach 300 Hz and a maximum force of 16 kN, while the latter four, featuring a maximum frequency and force of 10 kN and 50 Hz respectively, with a peak-to-peak displacement amplitude of 150 mm, are designed to replicate under-floor accelerations. Eventually, a methane burner can provide, on request, a 600 kg/h hot air mass-flow at a maximum temperature of 1 000 °C.

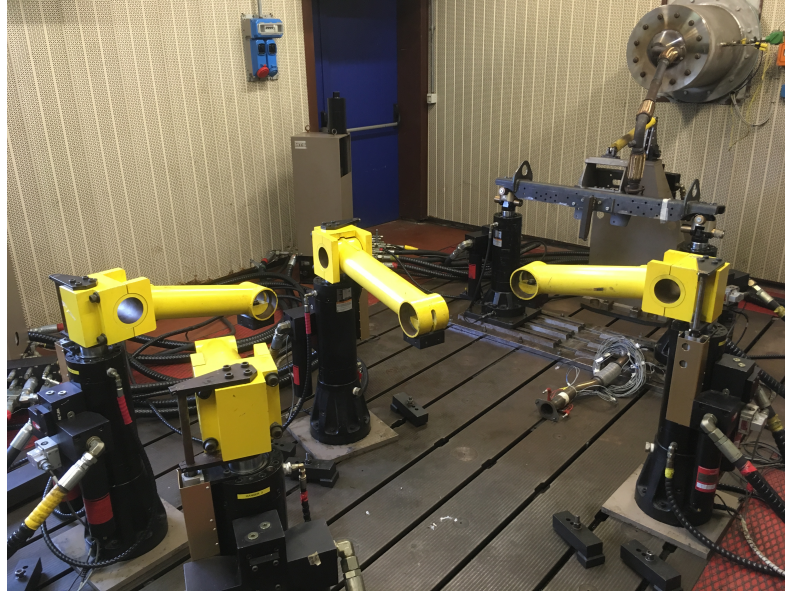


Figure B.1: *Road Simulation Bench room: the yellow arms are connected to hydraulic actuators reproducing vehicle body accelerations, while the three interlinked jacks, placed on the right of the picture below the gas burner simulate the vibrational behaviour of the engine*

For a conventional durability test, after the collection of data on the Proving Ground and the filtering of them, to remove non significant parts and shortening the test time, an instrumented exhaust line is mounted on the bench, in the same manner as under the vehicle: hydraulic actuators can be displaced to reproduce the position of the under-body counter-brackets. Once the set-up is complete, the bench starts a self-calibration: while moving one actuator at a time, it measures the intensities of the consequent accelerations and records them in an array of transfer functions (the coordinates of this matrix indicate the actuator moved and the accelerometer read). This process is repeated to minimize the error between the accelerations measured and the target the machine was supposed to measure. At the end of the calibration, the bench is aware of the type of displacement it has to provide in order to reproduce the same accelerations evidenced during the driving test, thus to replicate the durability test conditions, even on a new line of the same type not endowed with instruments.

Bibliography

- [1] Stefano Beretta. *Affidabilità delle costruzioni meccaniche: Strumenti e metodi per l'affidabilità di un progetto*. Springer Science & Business Media, 2010.
- [2] Antonio Gugliotta. *Elementi finiti*. Otto, 2002.
- [3] Tom Irvine. Power spectral density units:[g²/hz]. *Obtenido de Random Vibration & Power Spectral Density Page: <http://vibrationdata.com/tutorials2/psd.pdf>*, 2000.
- [4] Mayur Jagtap and Ashvin Dhoke. Topology optimization of exhaust mounting bracket. In *Tech Mahindra, Altair Technology Conference*, 2017.
- [5] Giovanni Petrucci. *Lezioni di costruzione di macchine*. 2007.
- [6] Rajadurai, Kavin, Rejinjose, Prabhakaran, and Rajeshraman. A system approach to dynamic characteristics of hanger rod in exhaust system. *International Journal of Innovative Science, Engineering & Technology*, 3(5), 2016.
- [7] S Rajadurai and N Suresh. Structural durability analysis of passenger car exhaust system using fpm approach in radioss.
- [8] S Rajadurai and N Suresh. Systematic fea study of passenger car exhaust system using radioss. *SAE Technical Paper*, 27(8):95–104, 2011.
- [9] Siemens. *Testing Knowledge Base Documents: <https://community.plm.automation.siemens.com/t5/Testing-Knowledge-Base>*.
- [10] Magneti Marelli R&D Exhaust Systems. *Magneti Marelli Internal Testing Procedure and Validating Norms*.
- [11] Marcella Turano, Fulvio Civera, Guilherme Figueiredo, Marco Margaria, and Andre Smith Pereira. Road simulation bench as a tool to reduce time and costs in comparison with proving ground testing-correlation study. Technical report, SAE Technical Paper, 2013.

- [12] John Van Baren. Fatigue damage spectrum—a new tool to accelerate vibration testing. *SOUND & VIBRATION*, page 15, 2015.
- [13] BS Vinutha et al. Study of static and frequency responsible analysis of hangers_ ampersandsignnbsp; _ ampersandsignnbsp; with exhaust system. *International Journal of Advances in Scientific Research and Engineering*, 3, 2017.

Acknowledgements

Before concluding this Thesis, I would like to thank all the people that sustained me not only for the realization of this project, but also during my whole Academic career.

First of all, I would like to thank Prof. Andrea Tonoli for having accepted to follow me in this project.

In the same manner, I want to thank Eng. Marco Nardi, who gave me the opportunity to undertake this path in Magneti Marelli, by integrating me in his Team, providing all the required tools: in absence of his commitment this project could not have been realized.

A special recognition goes to Doct. Federico Ogliaro, my tutor *ad honorem*, for his collaboration: since the first moment, he supervised my activity every single day with patience, illustrating me all the methods and procedures of his professional expertise with great competence.

In this perspective, I would also like to thank all the members of the Testing Department Team for their contributions both for the realization of this Thesis and for having increased my knowledge, illustrating me their working activities.

My particular gratitude goes to my Parents, who provided me an inestimable moral support and always supported my decisions, permitting the accomplishment of this career. Without your confidence, I would never have reached such an achievement.

Last but not least, my heartfelt thanks go to Joëlle, always by my side, who encouraged me with endless love and who trusts me more than I do. Your support has been fundamental, not only for the realization of this Thesis.